

THESIS FOR THE DEGREE OF DOCTOR OF PHILOSOPHY

# Aerodynamic Aspects of Propulsion Integration for Next-generation Commercial Aircraft

Vinícius Tavares Silva



Department of Mechanics and Maritime Sciences  
CHALMERS UNIVERSITY OF TECHNOLOGY  
Göteborg, Sweden 2023

Aerodynamic Aspects of Propulsion Integration for Next-generation Commercial Aircraft

VINÍCIUS TAVARES SILVA

ISBN 978-91-7905-844-9

© VINÍCIUS TAVARES SILVA, 2023.

Doktorsavhandlingar vid Chalmers tekniska högskola

Ny serie nr 5310

ISSN 0346-718X

Department of Mechanics and Maritime Sciences

Chalmers University of Technology

SE-412 96 Göteborg, Sweden

Telephone + 46 (0) 31 – 772 1000

Cover: Static pressure contours around an aircraft featuring over-wing mounted ultra-high bypass ratio engines (left). Over-wing nacelle scale model mounted in the Chalmers Low-speed Wind Tunnel (right).

Typeset by the author using L<sup>A</sup>T<sub>E</sub>X.

Printed by Chalmers Reproservice

Göteborg, Sweden 2023

*“There’s a better way to do it. Find it!”*  
- Thomas Edison

## ABSTRACT

### Aerodynamic Aspects of Propulsion Integration for Next-generation Commercial Aircraft

Thesis for the Degree of Doctor of Philosophy in Thermo and Fluid Dynamics

VINÍCIUS TAVARES SILVA

Department of Mechanics and Maritime Sciences

Division of Fluid Dynamics

Chalmers University of Technology

Propulsion integration is one of the most challenging aspects of aircraft design. It requires a multidisciplinary approach involving aerodynamics, propulsion, structures, weight, noise, and control systems. The constant push for lowering fuel burn and noise, and the recent goals for radically reducing the environmental impact of aviation drive the aviation industry to improve state-of-the-art technology and investigate innovative engine/aircraft integration solutions. A way to improve the specific fuel consumption of aircraft engines is by lowering the fan pressure ratio and increasing the bypass ratio. This is accompanied by larger fan diameters, and consequently increased nacelle weight and drag. The next-generation transport aircraft will feature engines substantially larger than those in-service, which will require shorter and lighter nacelles so that the engine performance benefits are not outweighed by an increased nacelle weight and drag. In this thesis, this problem is approached by developing new methods for the aerodynamic design of conventional and ultra-short nacelles, following a multi-point design methodology that considers the most critical operating conditions within the flight envelope. A computational fluid dynamics-based framework has been built to design nacelles and evaluate their aerodynamic performance. A comprehensive analysis of the aerodynamic aspects of nacelle design and the main parameters for the design of ultra-short nacelles are identified.

The installation of next-generation high-bypass turbofan engines also poses a major challenge to the aviation industry due to the limited space beneath the wings and stringent ground clearance constraints. Over-wing installed nacelles can be a potential solution for this problem, instead of the customary under-wing mounts. In this thesis, a framework for engine/aircraft integration aerodynamic design has been developed. The over-wing configuration is compared to conventional under-wing mounts in terms of aerodynamic performance. A novel method for wing redesign in the presence of the nacelle is proposed and an engine placement study is carried out.

In addition, low-speed wind tunnel tests were conducted for two scale configurations. The first was a standalone powered nacelle whereas the second was a half-span powered over-wing mounted nacelle configuration. The aim was to investigate the impact of the engine power setting and angle of attack on the flow field for low-speed operating conditions.

**Keywords:** Propulsion integration, Aerodynamics, Ultra-high-bypass-ratio engines, Ultra-short nacelles over-wing nacelle, Computational Fluid Dynamics, Low-speed testing.



## ACKNOWLEDGMENTS

I would like to start by thanking Anders Lundbladh for the stunning supervision, bright ideas, and long and insightful conversations. The depth of your knowledge never ceases to amaze me and our discussions have definitely made me a better researcher and engineer. I also owe my gratitude to Carlos Xisto, for the sharp and precise supervision, and for helping me to get back on my feet when things seemed hopeless. It has been nice to have someone to speak Portuguese with at the workplace.

Thanks to Tomas Grönstedt for giving me the great opportunity to pursue my Ph.D., for the supervision and guidance. To Olivier Petit for the supervision in my first year, and for helping me to fit in in Sweden. To Isak Jonsson, Valery Chernoray, and Petter Miltén for all the help in the lab. To Fabíola Costa for the research done together during her exchange period at Chalmers.

Thanks to Lars Davidson and all my colleagues in the Fluid Dynamics Division at Chalmers, for creating such a friendly and pleasant work environment. You most definitely made the Ph.D. student's experience a little bit more bearable. Thanks to Richard Avellán and the System Analysis and IP department at GKN Aerospace for welcoming me to the team and allowing me to finalize my Ph.D. in parallel.

Last but not least, the only reason why I could accomplish what I did is that I have the greatest family ever. Thanks, Mom and Dad for the unconditional support!

This research work was funded by the Swedish National Aviation Engineering Research Program, NFFP, supported by Swedish Armed Forces, the Swedish Defense Materiel Administration, Swedish Governmental Agency for Innovation Systems (VINNOVA) and GKN Aerospace. All the computations were performed using C3SE (Chalmers Center for Computational Science and Engineering) resources, provided by SNIC (Swedish National Infrastructure for Computing).

Vinícius Tavares Silva  
Gothenburg, May 2023

## LIST OF PUBLICATIONS

This thesis is based on the following appended papers:

**Paper A.** V. T. Silva, A. Lundbladh, O. Petit, and C. Xisto *Multipoint Aerodynamic Design of Ultrashort Nacelles for Ultrahigh-Bypass-Ratio Engines.*

**Paper B.** V. T. Silva, A. Venkatesh, M. Lejon, A. Lundbladh, and C. Xisto *Multipoint Aerodynamic Design of a Nacelle for an Electric fan.*

**Paper C.** V. T. Silva, A. Lundbladh, and C. Xisto *Aerodynamic Installation Effects of Over-the-wing Mounted Ultra-high-bypass Engines.* .

**Paper D.** V. T. Silva, A. Lundbladh, C. Xisto, and T. Grönstedt *Over-wing Integration of Ultra-high Bypass Ratio Engines: a Coupled Wing Redesign and Engine Position Study.*

**Paper E.** V. T. Silva, A. Lundbladh, C. Xisto, P. Miltén, and I. Jonsson *Powered Low-speed Experimental Aerodynamic Investigation of an Over-wing Mounted Nacelle Configuration.*

Other relevant publications:

**Paper F.** F. P. Costa, J. T. Tomita, V. T. Silva, N. Andersson, T. Grönstedt, and C. Bringhenti *Aerodynamic Analysis of Conventional and Boundary Layer Ingesting Propellers.*

## NOMENCLATURE

### Roman letters

$a$	– Lip length
$A$	– Area
$A_0$	– Captured streamtube area
$A_{hi}$	– Highlight area
$A_{fan}$	– Fan face area
$A_{ref}$	– Reference area
$A_{ex}$	– Exhaust area
$b$	– Lip height
$bp_i$	– Bernstein weighting coefficients
$BP_n$	– Bernstein polynomial of order n
$c$	– Chord
$c_{ref}$	– Reference chord
$C(\psi)$	– Class function
$C_d$	– Drag coefficient
$C_D$	– Discharge coefficient
$C_l$	– Lift coefficient
$C_{l_{max}}$	– Maximum lift coefficient
$C_p$	– Pressure coefficient
$DC_{60}$	– Total pressure distortion parameter
$D_{fan}$	– Fan diameter
$\mathbf{e}_d$	– Unity normal vector in the drag direction
$f_{cpr}$	– Lip control point radial position
$f_{cpx}$	– Lip control point axial position
$f_{le}$	– Non-dimensional leading edge radius of curvature
$f_{max}$	– Axial position of maximum diameter
$F_G$	– Stream gauge force
$F_{net}$	– Net propulsive force
$K_{i,n}$	– Binomial coefficients
$L_{CC}$	– Core cowl length
$L_{FC}$	– Fan cowl length
$L_I$	– Inlet length
$L_{nozz}$	– Nozzle length
$\dot{m}$	– Mass flow
$M$	– Mach number
$\mathbf{n}$	– Unity normal vector
$N$	– Class function exponents in a CST curve
$p$	– Static pressure
$p_t$	– Total pressure
$PR$	– Pressure ratio
$q$	– Dynamic pressure
$r_{fan}$	– Fan radius
$r_{hi}$	– Highlight radius

$r_{max}$	–	Maximum radius
$r_{th}$	–	Throat radius
$R_{le}$	–	Leading edge radius of curvature
$S(\psi)$	–	Shape function
$T$	–	Static temperature
$T_{net}$	–	Standard net thrust
$T_t$	–	Total temperature
$V$	–	Velocity magnitude
$\mathbf{V} = [u, v, w]$	–	Velocity vector

## Greek letters

$\alpha_i$	–	Airfoil incidence angle
$\beta_{cc}$	–	Core cowl boattail angle
$\beta_{te}$	–	Nacelle boattail angle
$\gamma$	–	Specific heat ratio
$\epsilon$	–	Airfoil camber angle
$\eta_{is}$	–	Isentropic efficiency
$\theta$	–	Local rotation angle for the reshaped airfoil
$\theta_d$	–	Droop angle
$\theta_{te}$	–	Trailing edge rotation
$\lambda$	–	Nozzle pressure ratio
$\xi$	–	Non-dimensional radial coordinate in a CST function
$\xi(\psi)$	–	Class shape transformation curve
$\xi_{te}$	–	Trailing edge radial coordinate modifier in a CST function
$\pi_d$	–	Intake pressure recovery
$\rho$	–	Density
$\psi$	–	Non-dimensional axial coordinate in a CST function
$\boldsymbol{\tau}$	–	Viscous stress vector
$\phi$	–	Wall and streamtube boundary forces
$\phi_{corr}$	–	Corrected mass flux
$\phi_{post}$	–	Post force
$\phi_{pre}$	–	Pre-entry force

## Subscripts and superscripts

*	–	Modified quantity
$\infty$	–	Freestream
0	–	Captured stream-tube entry station
2	–	Fan face
6	–	Low pressure turbine exit
13	–	Fan exit
A	–	Airframe
bn	–	Bypass nozzle
cc	–	Core cowl
crit	–	Critical condition at which the flow becomes sonic

cn	–	Core nozzle
FC	–	Fan cowl
hi	–	Highlight
id	–	Ideal flow property
I	–	Inlet
NAC	–	Nacelle
net	–	Net quantity
max	–	Maximum
nozz	–	Nozzle
ref	–	Reference
spin	–	Spinner
targ	–	Target
te	–	Trailing edge
th	–	Throat

## Acronyms

AoA	–	Angle of attack
BC	–	Boundary condition
BPR	–	Bypass ratio
CFD	–	Computational fluid dynamics
CRM	–	Common research model
CST	–	Class shape transformation
EDF	–	Electric ducted fan
FPR	–	Fan pressure ratio
MFR	–	Mass flow ratio
MHB	–	Maximum half-breadth
OWN	–	Over-wing nacelle
RANS	–	Reynolds-averaged Navier-Stokes
SST	–	Shear-stress transport
UHBPR	–	Ultra-high bypass ratio
UWN	–	Under-wing nacelle
WB	–	Wing body
WBPN	–	Wing body pylon nacelle



# Contents

<b>I</b>	<b>Introductory chapters</b>	<b>1</b>
<b>1</b>	<b>Introduction</b>	<b>3</b>
1.1	Objectives . . . . .	5
<b>2</b>	<b>Propulsion Integration: General Aspects and Previous Work</b>	<b>7</b>
2.1	Aerodynamic Design of Nacelles . . . . .	9
2.2	Aerodynamic Aspects of Propulsion Integration . . . . .	10
2.2.1	Under-wing nacelles . . . . .	10
2.2.2	Over-wing nacelles . . . . .	12
2.3	Previous Work and Research Gaps . . . . .	13
2.3.1	Nacelle Design and Aerodynamics . . . . .	13
2.3.2	Fan Modelling . . . . .	14
2.3.3	Propulsion Integration . . . . .	14
2.3.4	Wind Tunnel Testing . . . . .	16
<b>3</b>	<b>Methods</b>	<b>17</b>
3.1	Geometry Generation . . . . .	17
3.1.1	Class Shape Transformation Method . . . . .	17
3.1.2	Nacelle Parametrization . . . . .	18
3.1.3	3D Nacelle Geometry Generation . . . . .	21
3.1.4	Integration With the Aircraft . . . . .	22
3.1.5	Wing Reshaping . . . . .	22
3.2	Numerical Approach . . . . .	24
3.2.1	Standalone Nacelles . . . . .	24
3.2.2	Fan Face Boundary Condition . . . . .	26
3.2.3	Integrated Configurations . . . . .	29
3.3	Performance Metrics . . . . .	31
3.3.1	Thrust and Drag Bookkeeping . . . . .	31
3.3.2	Performance of Inlets and Nozzles . . . . .	34
3.4	Nacelle Design Process . . . . .	35
3.4.1	Operating Conditions . . . . .	37
3.5	Aircraft Equilibrium of Forces . . . . .	37

---

<b>4</b>	<b>Experimental Investigation</b>	<b>39</b>
4.1	Test Rig 1: Standalone Nacelle . . . . .	39
4.1.1	Description . . . . .	39
4.1.2	Results . . . . .	41
4.2	Test Rig 2: Over-wing Nacelle Configuration . . . . .	43
<b>5</b>	<b>Summary of Papers</b>	<b>45</b>
5.1	Paper A . . . . .	45
5.1.1	Summary and Discussion . . . . .	45
5.1.2	Division of work . . . . .	46
5.2	Paper B . . . . .	46
5.2.1	Summary and Discussion . . . . .	46
5.2.2	Division of work . . . . .	47
5.3	Paper C . . . . .	47
5.3.1	Summary and Discussion . . . . .	47
5.3.2	Division of work . . . . .	47
5.4	Paper D . . . . .	48
5.4.1	Summary and Discussion . . . . .	48
5.4.2	Division of work . . . . .	48
5.5	Paper E . . . . .	49
5.5.1	Summary and Discussion. . . . .	49
5.5.2	Division of work . . . . .	49
5.6	Paper F . . . . .	50
5.6.1	Summary and Discussion . . . . .	50
5.6.2	Division of work . . . . .	50
<b>6</b>	<b>Concluding Remarks</b>	<b>51</b>
6.1	Nacelle Design . . . . .	51
6.2	Integration With the Aircraft . . . . .	52
6.3	Experimental Investigation . . . . .	53
	<b>Bibliography</b>	<b>55</b>
<b>II</b>	<b>Appended papers</b>	<b>63</b>
<b>A</b>	<b>Multipoint Aerodynamic Design of Ultrashort Nacelles for Ultrahigh-Bypass-Ratio Engines</b>	<b>65</b>
<b>B</b>	<b>Multipoint Aerodynamic Design of a Nacelle for an Electric fan</b>	<b>85</b>
<b>C</b>	<b>Aerodynamic Installation Effects of Over-the-wing Mounted Ultra-high-bypass Engines</b>	<b>105</b>
<b>D</b>	<b>Over-wing Integration of Ultra-high Bypass Ratio Engines: a Coupled Wing Redesign and Engine Position Study</b>	<b>121</b>



---

E	Powered Low-speed Experimental Aerodynamic Investigation of an Over-wing Mounted Nacelle Configuration	141
F	Aerodynamic Analysis of Conventional and Boundary Layer Ingesting Propellers	157



# Part I

## Introductory chapters



# Chapter 1

## Introduction

In civil aviation, there has been a constant push for the reduction of fuel burn, noise, and environmental impact. Each new aircraft generation has improved fuel burn and emissions by around 15-20%, compared to its predecessor, by improving engine technology and aerodynamic efficiency. With the envisaged air traffic growth and growing environmental impact, aviation has recently become the object of higher scrutiny and it has been acknowledged that further action is necessary on the field. The European aviation industry has set a target for net zero  $CO_2$  emissions from all flights within and departing from the European Union to be achieved by 2050 and established an ambitious decarbonization roadmap [1]. To fulfill such challenging objectives, the consistent incremental improvements will need to be accompanied by radically novel propulsion and airframe technologies. Aircraft manufacturers and research institutions are currently working on new revolutionary aircraft and propulsion concepts that aim at drastically reducing the environmental impact of aviation. Concepts such as the blended-wing-body [2], the truss-braced wing [3], and boundary layer ingestion [4], [5] are examples of novel aircraft configurations being widely investigated. Moreover, novel propulsion systems such as hybrid-electric, full-electric, and hydrogen-powered aircraft, as well as new engine architectures, such as the OpenFan [6], are potentially large steps on the long road toward the decarbonization of air transport. Nevertheless, such radically new technologies require a long time to mature or can eventually come to be unfeasible solutions, and thus it is crucial that conventional tube-and-wing configurations keep evolving at an accelerated rate. This can be done by improving airframe aerodynamics, using more advanced and lighter materials, and by developing more fuel-efficient engines.

To improve the overall efficiency of aero-engines, it is necessary to simultaneously enhance the engine's thermal and propulsive efficiencies. The former can be raised by improving the performance of the core components, by increasing the burner exit temperature and the overall pressure ratio. The latter can be achieved by lowering the fan pressure ratio (FPR) and raising the bypass ratio (BPR). The next-generation turbofan engines are expected to operate with cruise BPRs of 15 and greater, referred to as ultra-high bypass ratio (UHBPR) engines, and FPRs lower than 1.4. One of the technologies that might allow this to become reality is the geared-fan architecture, which features a gearbox between the fan and the core

engine. In addition, substantial noise reduction can be obtained with low FPR and low fan speeds [7]. However, a direct result of increasing the BPR, is larger fan and nacelle diameters and, consequently, higher nacelle weight and drag. When the engine size increases substantially, the fuel burn benefit from a higher engine propulsive efficiency is outweighed by the increased nacelle drag. The geared-fan technology allowed the point of optimum fuel burn to be shifted downward, by reducing the fan's rotational speed, as can be seen in Fig. 1.1. As the engine size is expected to keep raising, advanced nacelle designs, with shorter inlets and exhaust nozzles, are required so that the gain in propulsive efficiency is not outweighed by the higher installation drag and weight. With the advent of new nacelle, fan, and core technologies, combined with novel advanced design methods, larger engines can possibly be designed without the current performance penalties. A schematic representation of the engine technology evolution is shown in Fig. 1.1. It is clear that the engine size and BPR must increase for reduced fuel burn and noise, and this will require the inlet to be shortened, i.e., the inlet over fan diameter ratio ( $L_I/D_{fan}$ ) to decrease.

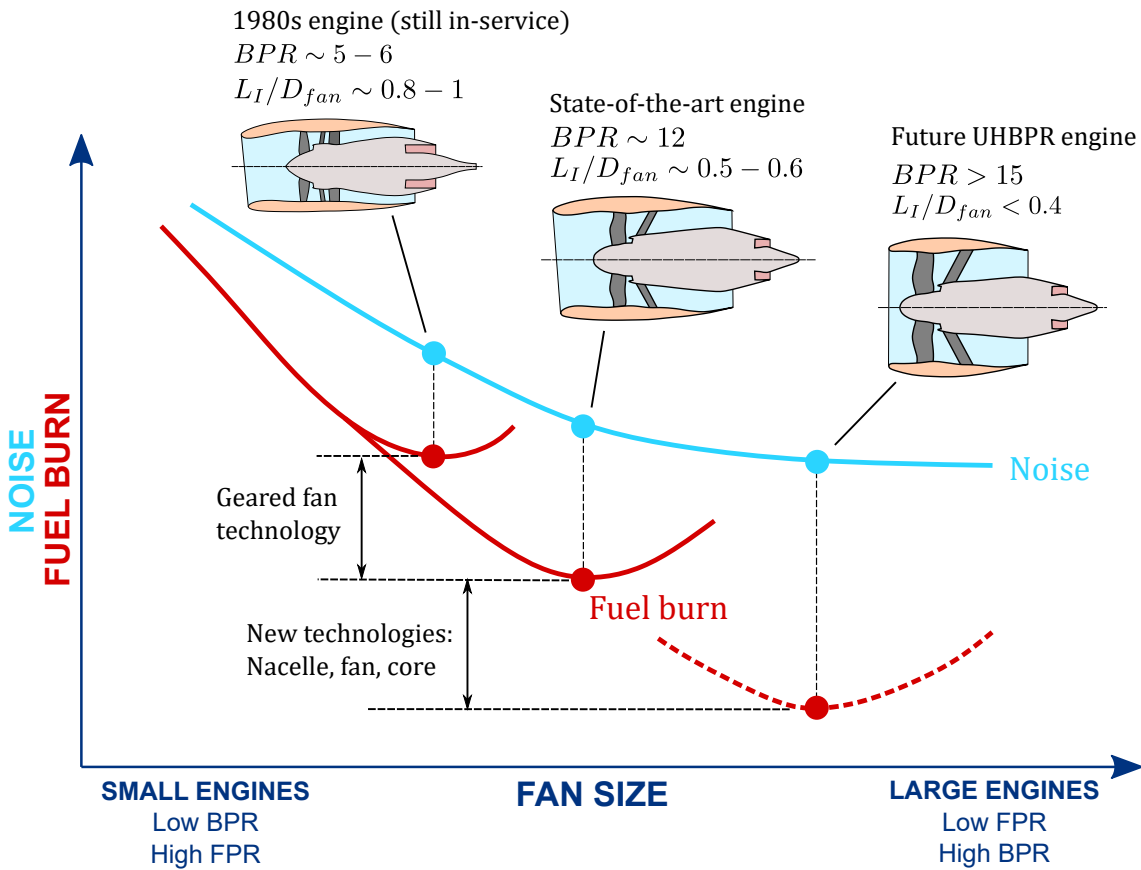


Figure 1.1: Technology evolution of turbofan engines for commercial aircraft. Adapted from [8].

State-of-the-art turbofan engines feature intakes with  $L_I/D_{fan}$  between 0.5 and 0.6. However, intakes for future aero-engines will be shorter, likely having a  $L_I/D_{fan}$  between 0.3 and 0.4. As inlets shorten, the fan-inlet coupling gets stronger and

the nacelle design becomes substantially more challenging, especially for low-speed and high-incidence conditions. Since short inlets have reduced internal diffusion capability, they are more likely to ingest highly distorted flows, and more susceptible to boundary layer separation, leading to poor performance and engine instability. In the thesis, the aerodynamic design of ultra-short nacelles for future aero-engines is addressed in detail.

The vast majority of civil aircraft feature engines mounted under and upstream of the wings, since such placement usually provides lower installation drag than other integration choices. History shows that over the years the engines' axial location has been moved forward and engines have become more closely coupled with the wing [9]. Positioning the engines forward generally grants a lower installation drag, whereas installing them closer to the wing is merely a consequence of higher BPR engines and nacelle diameters. The issues with the integration of high-bypass turbofan engines date back to the 80s. The limited space available underneath the wings, summed with strict ground clearance constraints makes it a hard multidisciplinary problem. To accommodate large engines, long and heavy landing gears might be necessary, increasing the aircraft's weight and drag. Moreover, as in the B737, the lower part of the nacelle sometimes needs to be flattened so that the engine will meet the ground clearance requirements.

Up to this day, engineers have found solutions and compromises that made it possible for the customary under-wing installations to prevail. Nevertheless, under-wing integration might not be a suitable solution for future UHBPR engines, mostly due to the prohibitively large and heavy landing gears necessary. Other types of integration can offer the solution to such a problem, such as high wings with under-wing mounted engines, low wings with over-wing mounted engines, or embedded engines, for which the engines are partially buried into the fuselage. This work, in particular, addresses the aerodynamic aspects of propulsion integration for UHBPR turbofan engines positioned over the wings, in comparison to conventional under-wing mounts.

## 1.1 Objectives

This thesis tackles two major problems faced by the civil aviation industry regarding the propulsion integration of next-generation aero-engines. The first is the design of ultra-short nacelles for UHBPR turbofan engines. The second is the integration of UHBPR engines with the airframe. The goals of this thesis are to provide novel CFD-aided design methods for the integration of next-generation aero-engines, conduct a thorough investigation of the aerodynamics aspects of nacelle design and its integration with the aircraft, and to investigate the feasibility of an innovative over-wing mounted nacelle configuration. Such goals can be better split into two fundamental parts: 1) design of uninstalled nacelles and 2) integration of nacelles with the airframe. The first part of this work will be achieved through the completion of the following objectives:

- Establishing a novel methodology for the multi-point design of ultra-short nacelles for UHBPR turbofan engines.

- Developing a new method to reproduce the intake-fan coupling at critical operating conditions that does not rely on the geometry of the fan blades or on extensive data for calibration.
- Studying the flow field around nacelles under operating conditions considered to be critical for the engine's performance and stability.
- Identifying the major design parameters in each of the operating conditions and how they impact the flow field and nacelle aerodynamic performance.
- Designing geometries that provide good performance trade-offs between the high and low-speed flow conditions and highlighting important decisions to be taken during the design procedure.

The second part of this work will be achieved by accomplishing the following goals:

- Conducting a thorough investigation of the aerodynamic impact of installing UHBPR engines over the wings.
- Developing a novel method for reshaping the wing of an over-wing nacelle (OWN) configuration.
- Performing an engine position sensitivity study coupled with the developed wing reshaping method for the OWN configuration.
- Investigating in detail the coupling between aerodynamics and propulsion, and the interference effects between wing nacelle and pylon.
- Comparing the best OWN installation obtained with a baseline under-wing nacelle (UWN) configuration.

Another goal of this work is to conduct low-speed powered experimental investigations on an uninstalled and an over-wing mounted nacelle configuration, to complement and validate the results obtained from the numerical studies.



## Chapter 2

# Propulsion Integration: General Aspects and Previous Work

A turbofan engine for commercial aircraft is enclosed by a nacelle and attached to the wing by means of a pylon. Figure 2.1 shows an illustration of an aircraft with under-wing mounted nacelles, attached to the wing via a pylon. A two-stream turbofan nacelle is comprised of an inlet, an external cowl, a bypass nozzle, and a core nozzle. The part of the nacelle that covers the core engine is referred to as the core cowl. The nacelle also contains a braking mechanism referred to as the thrust reverser, to reduce the landing distance. Modern turbofan engines usually feature a cascade-type thrust reverser, in which the rear part of the cowl and the bypass nozzle slide axially to allow the bypass flow to change its direction. Moreover, nacelles comprise acoustic liners for noise damping. Two-stream turbofans can feature chevron nozzles which are serrated edges, in a saw-tooth pattern, at the trailing edge of the nozzles, to reduce the jet blast noise. Figure 2.2 shows a schematic representation of a two-stream turbofan nacelle longitudinal section. The top half shows the forward thrust mode and the bottom half shows the reverse thrust mode.

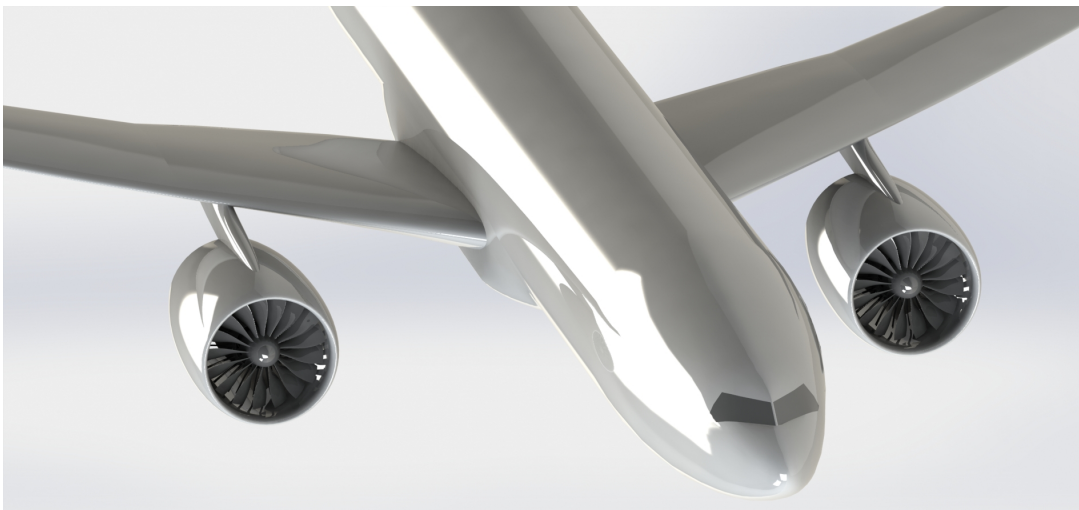


Figure 2.1: Under-wing mounted nacelles attached to the airframe by means of a pylon.

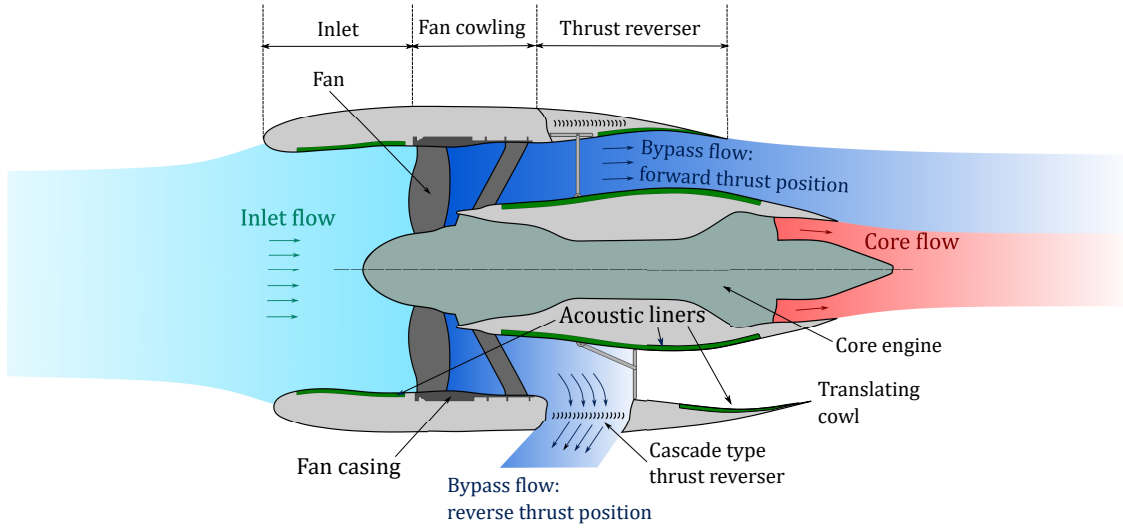


Figure 2.2: Schematic representation of a nacelle for a two-stream high-bypass turbofan. The top half shows the forward thrust mode and the bottom shows the reverse thrust mode.

A well-designed inlet is essential for the engine to operate safely and efficiently during the entire flight envelope. The intake system should be designed to fulfill the following requirements [10]:

1. Provide an adequate fan face Mach number and engine mass flow rate during the entire mission.
2. Provide a smooth flow to the fan, with a higher pressure recovery and low distortion levels for the entire flight envelope.
3. Provide low installation drag and weight.
4. Provide acoustic damping of the fan noise.
5. Allow for engine thrust growth.

The bypass and core nozzles have the main function of accelerating the cold and hot streams, converting the fluid internal energy into kinetic energy and thus propulsive force. Nozzles for aero-engines should be designed to meet the flowing criteria [10]:

1. Efficient expansion of gases to the free stream.
2. Low installation drag.
3. High-performance reverse thrust capabilities.
4. Low weight.

In the next sections, firstly, the major aspects of nacelle aerodynamic design are addressed. Secondly, the aerodynamic aspects of engine aircraft integration are discussed. Lastly, some of the major research work in the field of propulsion integration are summarized.

## 2.1 Aerodynamic Design of Nacelles

The design of a turbofan nacelle requires several compromises since the optimum shape will be different for distinct operating conditions within the flight envelope [11], [12]. Figure 2.3 shows a schematic representation of the flow field under different operating conditions and some of the possible flow field characteristics.

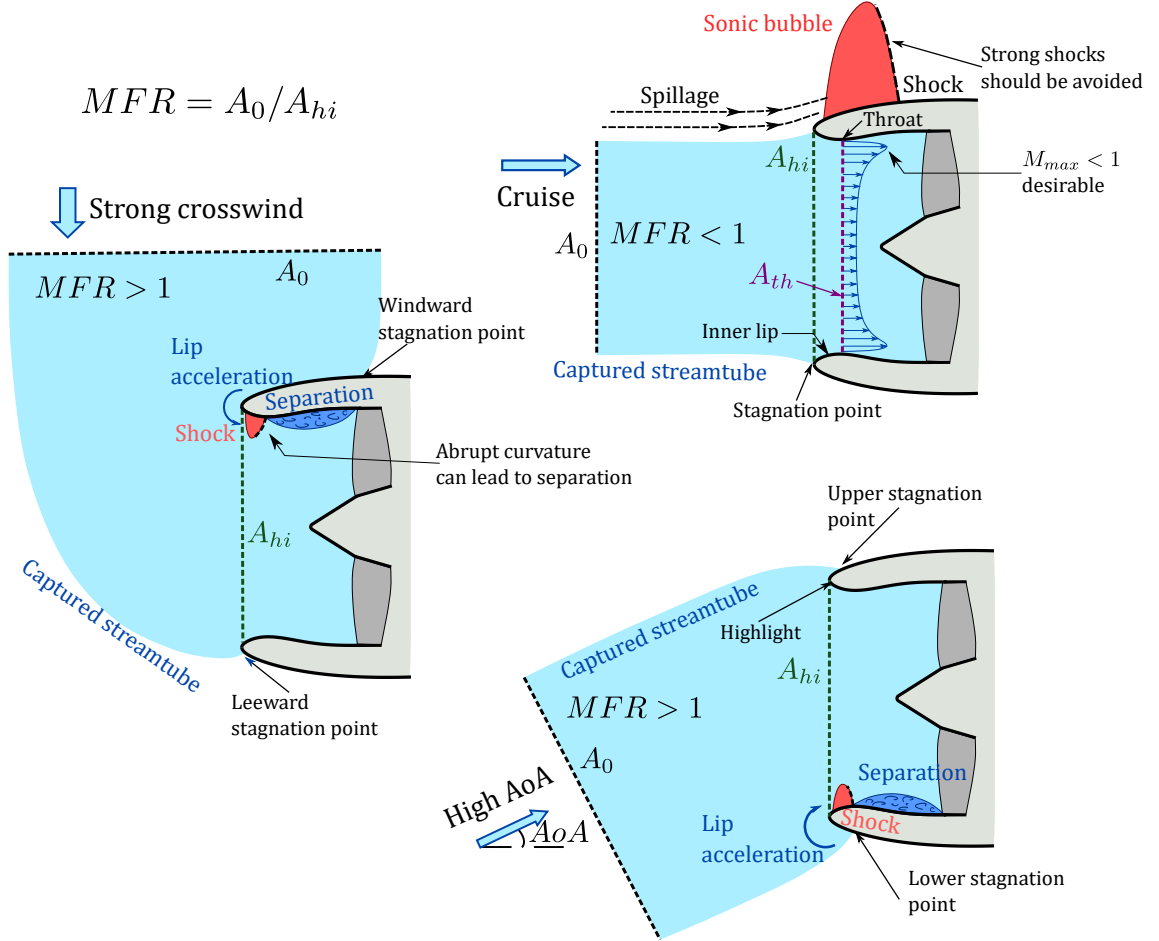


Figure 2.3: Schematic representation of the flow field for different operating conditions: cruise (side view), high-incidence (side view), and crosswind (top view).

For cruise the focus should be minimizing drag, therefore, the supersonic velocities at the fan cowling should be limited, and shock waves should be avoided when possible since they are accompanied by a significant increase in wave drag. Internally in the inlet, shock waves can also be formed, causing excessive boundary layer thickening and increased loss in intake pressure recovery  $\eta_i$ . In the most severe cases, shock-induced separations can occur, and thus the throat area should be selected to avoid shock formation [11]–[13].

A reference aerodynamic parameter for the inlet is the mass flow ratio, MFR, which is defined as the ratio between the streamtube captured area  $A_0$  and the highlight area  $A_{hi}$ . Typical values of MFR will vary between 0.7 and 0.8 for cruise.

At low speeds, the MFR will be larger than unity and the highest velocities will occur internally in the inlet. Particularly at high incidence, the lower stagnation point will be somewhere outside the lip and thus the flow needs to accelerate around the lip, which results in strong shocks downstream of the highlight position. This frequently results in shock-induced separation. For crosswind, the MFR is the greatest and the windward stagnation point is now located somewhere at the fan cowling. This requires the flow to be severely deflected in order to enter the inlet duct. Two types of separation can occur in this case: the first happens for low speeds and is primarily driven by excessive diffusion, starting near the highlight position; the second takes place for high fan speeds and high inlet mass flows, when a shock wave is formed internally in the windward lip, and the strong adverse pressure gradient causes the flow to separate.

The conflicting requirements existing for different flight conditions result in an asymmetric nacelle shape. The inlet is thus thinner on its top part to avoid excessive wave drag, whilst its lower part is thicker and rounder, to prevent high-incidence separation and to alleviate distortion.

Excessive drag can result from the bypass jet and the external stream interaction. If the nozzle is choked, the exhaust pressure will be higher than the ambient pressure. Strong adverse pressure gradients can develop in the fan cowl, generating a small separation region and increasing drag substantially. The drag developed by the rear part of the fan cowl is termed boat tail drag and a proper boat tail angle  $\beta_{te}$  should be selected to minimize it.

Engine inoperative conditions, such as idle and windmilling, should also be investigated during the nacelle design process. For such conditions, the inlet mass flow and MFR are very low, causing the flow to stagnate internally in the inlet. The uncaptured flow has to accelerate around the lip, creating strong pressure gradients at its external part. If the lip and cowling are not properly shaped, external flow separation can occur.

## 2.2 Aerodynamic Aspects of Propulsion Integration

### 2.2.1 Under-wing nacelles

Most modern commercial aircraft feature engines placed under and upstream of the wings. History shows that a forward engine placement is generally beneficial for minimizing installed drag. Moreover, due to the large fan diameters, modern aero-engines need to be integrated closely coupled with the wings, and thus the vertical gap between the engine and wings has been decreasing as time progresses. It is well known that the presence of the nacelle significantly impacts the flow field around the wing and vice versa, and consequently, the overall profile, induced, and wave drag will significantly differ for the installed configuration. Since the wing, nacelle, and pylon shapes interact with each other, the wing can be better optimized in the presence of the nacelle.

Some of the most common aerodynamic aspects that should be taken into account during the engine integration process are pointed out in Fig. 2.4 and described as

follows:

- The design of an installed under-wing inlet differs from that of an isolated one since the inlet should be drooped for better alignment with the wing upwash and drag reduction at cruise. The upwash also impacts the nacelle incidence at low-speed conditions such as takeoff.
- The fan cowl shock is affected by the presence of the pylon. The flow tends to stagnate near the pylon's intersection with the nacelle, and accelerate over the top of the pylon, possibly reaching supersonic speeds. Shallow pylon/cowl intersection angles are generally a good solution to avoid excessive stagnation and reduce wave drag.
- For an under-wing mount, the exhaust jet affects the flow around the wing. As the jet velocity is higher than that of the freestream, it counters the natural circulation around the wing and leads to some local lift loss. The lift is recovered by flying at higher AoA, and this results in a higher configuration drag. The additional drag caused by the jet's influence on its surroundings is referred to as blowing drag [9]. Lower FPRs and jet velocities are beneficial for reducing blowing drag.
- The shape of the exhaust system has a high impact on interference drag. A conical external core cowl has been shown to perform better than a curved exhaust system for two stream high-bypass turbofans [9].
- A forward engine placement is generally beneficial for reducing installed drag, however, weight and manufacturing costs are also taken into account when selecting the engines' axial position.
- The exhaust shape and length are influenced by noise considerations and by the design of the thrust reversers.

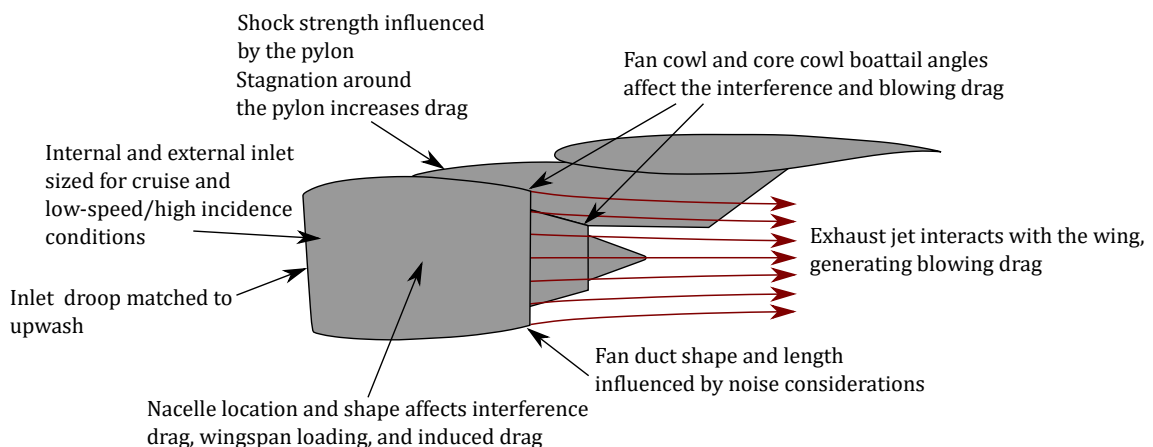


Figure 2.4: Aerodynamic aspects affecting under-wing nacelle installation.

### 2.2.2 Over-wing nacelles

As previously mentioned, over-wing mounted nacelles are a potential solution for the integration of UHBPR engines. However, in an OWN configuration, the engine considerably disturbs the flow on the wing's upper surface and a strong coupling between aerodynamics and propulsion is observed. At cruise conditions, a high-pressure zone is formed ahead of the nacelle, which locally increases the pressure on the wing's upper surface and can potentially cause a severe loss in lift. To recover the lift, the aircraft has to fly at a higher AoA, leading to an increased wing shock strength and substantially higher wave drag. Figure 2.5 illustrates such a phenomenon by comparing a conventional UWN installation to an OWN mount. The high-pressure zone formation and stronger shock for the OWN configuration can be easily observed from the  $C_p$  contours. This problem can be solved, however, it requires advanced coupled design and optimization techniques that consider the interaction and interference effects between the nacelle, wing, and pylon. Papers C and D bring a detailed analysis of OWN integration aerodynamics and a novel method for reshaping the wing in the presence of an over-wing mounted nacelle.

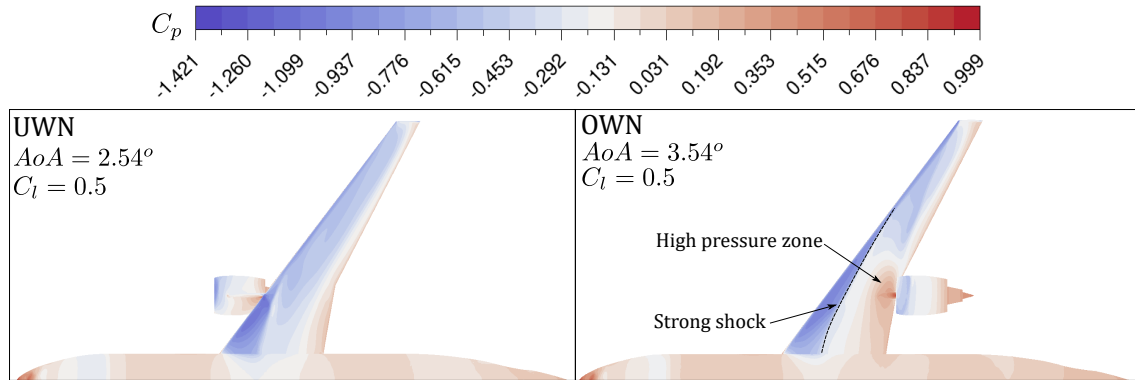


Figure 2.5: Pressure contours for under-wing and over-wing mounted nacelles. The high-pressure zone and stronger wing shock are highlighted for the OWN configuration.

A unique characteristic of over-wing mounted nacelles is the powered lift produced at low speeds. The high-pressure zone shown in Fig. 2.5 is caused because, at cruise conditions, the inlet MFR is less than unity, meaning that diffusion occurs in the captured streamtube and the pressure ahead of the nacelle increases. At low speeds, the engine operates at a higher power setting, and the MFR is higher than one, meaning that the streamlines entering the engine present a converging pattern, and the flow accelerates ahead of the engine. A low-pressure zone is formed upstream of the engine and on the upper surface of the wing. This generates a lift benefit that is referred to as powered-lift [14], [15]. Figure 2.6 shows the MFR effect on the flowfield upstream of the nacelle for two different power settings. In paper E powered low-speed experimental tests were carried out to investigate the impact of the engine power setting on the wing lift for an OWN configuration.

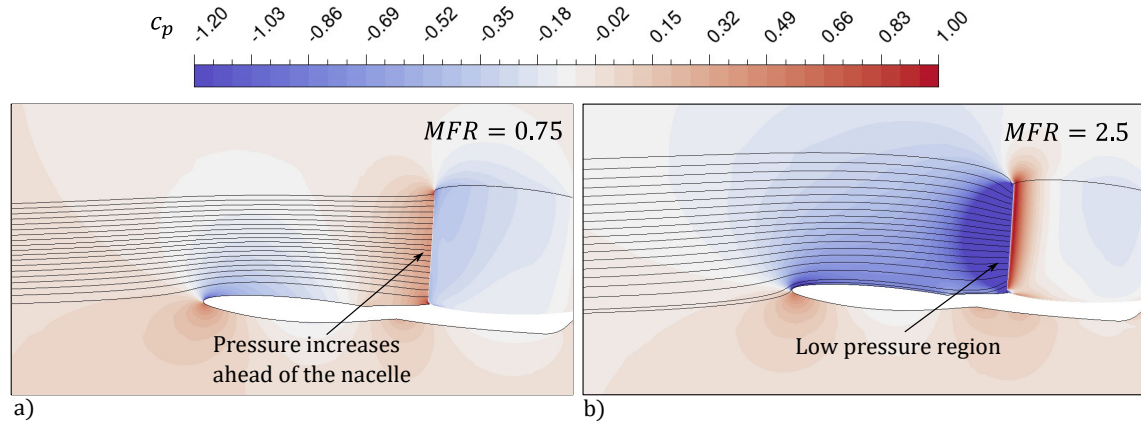


Figure 2.6: Power setting effect on the flowfield upstream of the nacelle for a) MFR=0.75 and b) MFR=2.5.

## 2.3 Previous Work and Research Gaps

### 2.3.1 Nacelle Design and Aerodynamics

The design of high-bypass ratio turbofan nacelles has been subject of research since the early 60's. The methods for shaping nacelles can be split into two categories: parametric and inverse design. The former consists of building the nacelle based on pre-defined aerodynamic shapes, such as airfoil profiles or splines [16]–[25]. The latter consists of adapting the nacelle form for attaining a targeted pressure distribution [26]–[29]. As the civil aero-engines get larger, the more crucial it becomes to severely reduce nacelle drag. This can be done either by shortening the inlets and exhaust nozzles [30]–[32], by achieving natural or hybrid laminar flow over the nacelles [33]–[37], or a combination of both.

Considerable achievements in modern nacelle design were reached over the last decade. Cristie et al. [38], [39] and Lundbladh et al. [40] have developed new Class Shape Transformation (CST) based approaches for designing nacelle and intake aero-lines, and Tajero et al. [41]–[43] have developed CST-based methods for 3D nacelle shape multi-objective optimization. Furthermore, CST curves were also widely used for exhaust nozzles design and optimization [44]–[46]. Peters et al. [30] have presented a spline-based framework for designing nacelles with ultra-short inlets and assessed the performance of different short inlet candidates compared to a standard length baseline. Rainer Schnell et al. [31] presented coupled fan-intake design methodology for potential application to ultra-short intakes for UHBPR engines. Extensive research has been conducted on nacelles subjected to crosswinds [47]–[50] and a few studies considering crosswind effects on short inlets can be found in the literature [30]–[32].

Although there is no shortage of research on modern nacelle design, there are still questions on how far technology can go, i.e., how short nacelles can be designed, and how much fuel burn benefit could be attained by shortening them. Furthermore, there is still a lack of research on how critical off-design operation conditions such as low speed/high angle of attack (AoA) and crosswind could impact the 3D design of

next-generation turbofan nacelles, specifically the ones with ultra-short inlets. Paper A [51] and Paper B [52] of this thesis attempt to answer some of these questions. The former provides a novel CST-based methodology for the multi-point design of ultra-short nacelles. The design procedure considers 3D effects of both asymmetric geometries and asymmetric flow fields under the most critical conditions that are expected to occur for a given aircraft mission, such as cruise, high AoA, and crosswind. The latter provides a multi-point aerodynamic design of a 3D nacelle for an electric fan considering cruise and end-of-runway takeoff conditions.

### 2.3.2 Fan Modelling

The aerodynamic design of nacelles requires that the fan-inlet coupling is properly captured. Three-dimensional asymmetric nacelle flows require full annulus fan simulations, however, such computations have a high computational cost and normally are not feasible during the preliminary design and optimization stage, due to the large number of computations required. It is a common practice to mimic the fan behavior by means of traditional boundary conditions, actuator discs, or body force models. The use of simple boundary conditions, such as setting a constant static pressure at the fan face, is a reasonable approach for conditions for which the incoming flow level of uniformity is high. However, highly distorted flows require the fan to respond locally to spatial changes in total pressure. Actuator disk boundary conditions [53], [54] and body force models [55]–[59] have been successfully implemented to reproduce the behavior of fans ingesting asymmetric flows. Nonetheless, such models usually require either fan geometry information, or more detailed computations or experiments to be calibrated with. It is worth mentioning that some body-force models which require low levels of input detail have been implemented [55], [59], however, they are not reliable for extreme off-design conditions, where the incoming flow can be highly distorted, or even separated.

During the preliminary stage of nacelle design, the aerodynamicist might have limited or no access to the fan geometry or its performance data, therefore a simpler alternative to the methods mentioned above would be of great convenience. In this thesis, the modified parallel compressor method (MPC) was developed as a novel boundary condition for the fan. The method is aimed to be applied at the preliminary stages of nacelle design and requires only a generic fan map or speed line as input. The MPC method is derived from the classical parallel compressor theory [60]–[63], and it has been adapted to be used in CFD computations. The method is described in detail and validated in Paper A. Moreover, it is applied to the simulations carried out in Paper B.

### 2.3.3 Propulsion Integration

The integration of high-bypass turbofans is one of the most interesting and challenging aspects of aircraft design. It often requires multidisciplinary approaches including aerodynamics, propulsion, structures, weight, noise, fluid-structure-interaction, and so forth. A great summary of some of the most common challenges encountered in the field of propulsion integration is described in Ref. [9], where the integration process of the Boeing 777 is described for engines of different manufacturers, and



the major challenges and necessary compromises are highlighted. Furthermore, early propulsion integration Boeing studies on high transonic speeds are described in [64], and Ref. [65] demonstrates the benefits of using viscous numerical methods for achieving better engine installation aerodynamics.

Recently, CFD simulations have been widely used to better evaluate the aerodynamic effects of propulsion integration for UHBPR turbofan engines. The effect of the nacelles' axial and vertical placement on the aerodynamic performance of UWN configurations is evaluated in Refs. [66]–[69]. Magrini et al. [70] and Sanches Moreno et al. [71] conducted nacelle shape optimizations in the presence of the airframe, and the design of asymmetric integrated exhaust systems was conducted by Otter et al. [72].

The integration of UHBPR engines requires nacelles close-coupled with the wing due to the limited space underneath the wings and ground clearance constraints. As the engines grow larger, longer and heavier landing gears may be necessary, resulting in additional weight and drag. Over-wing mounted nacelles would eliminate the ground clearance issue and, potentially reduce noise due to acoustic shielding from the wings. The OWN installation acquired a bad reputation in the past since it would be usually outperformed by conventional UWN configurations [73]. However, with the advance in CFD techniques, it is possible to design better OWN aircraft by considering the interactions between the wing, nacelle, and pylon, and thus new attention has been given to such configurations. A study by Hooker et al. [74] is noteworthy, as it carried out various wing shape and nacelle position optimizations for different wing types, nacelle placement, and BPRs. The results indicate that the optimal configuration is an OWN installation, which features a low wing and trailing edge mounted engines. This configuration has the potential to improve aerodynamic efficiency by up to 5% compared to a traditional UWN setup.

Lange and Rudnik [75] have achieved a drag reduction of 11% by optimizing the nacelle' axial and vertical positions in an OWN configuration, compared to the baseline location. Wegener [76], and Wegener and Lange [77], have studied fuselage and wing-mounted OWN installations, and conducted wing shape and twist distribution optimizations. Compared to a baseline UWN case, the optimum wing and fuselage-mounted configurations had approximately 20% and 9% additional drag, respectively. Ahuja et al. [78] carried out a sensitivity study of drag, lift and intake pressure recovery to variations in the nacelle location for an OWN configuration. The wing shape was optimized for the best nacelle position and a 20% drag reduction was obtained, compared to the baseline configuration. However, the optimized OWN aircraft still had a drag 5% higher than that of the baseline UWN configuration.

The integration of over-wing mounted nacelles is a complex problem, involving a strong coupling between aerodynamics and propulsion. The studies mentioned above reinforce the need for novel design methods capable of capturing the interactions between the pylon, wing, and nacelle. In this thesis, Paper C [79] brings an aerodynamic evaluation of an OWN configuration compared to a conventional UWN mount, whilst Paper D reports a novel method for wing reshaping in the presence of an over-wing mounted nacelle. Moreover, Paper E describes powered low-speed tests carried out at the Chalmers's low-speed wind tunnel, for an OWN configuration.

### 2.3.4 Wind Tunnel Testing

Typically, transonic wind tunnel tests are performed for flow-through nacelle configurations since the results have been shown to reproduce real flight conditions reasonably. Experimental investigations for the wing-body-pylon-nacelle (WBPN) NASA Common Research Model (CRM) were conducted in two different transonic wind tunnels, for typical cruise conditions [80]. Although unpowered tests can provide useful information about the nacelle's low-speed aerodynamic performance, as shown by Zawislak et.al [81], it is known that the fan power setting has a substantial impact on the flow field and on inlet distortion at low-speed operation. Larkin and Schwiger [82] demonstrated that a flow-thorough inlet can decrease the separation-free angle of attack from  $4^\circ$  to  $3^\circ$  compared to a powered setup. Kusunose et al. [83] have developed a wake integration method to consider the powered engine effects, which was applied to low-speed powered tests. Brune [84] has compared the spanwise profile and induced drag for aircraft models with powered and flow-through nacelles using a wake survey integration method. The results are similar for the outboard wing but differ substantially in its inner portion. Lastly, Lockheed Martin conducted powered low-speed testing of the Hybrid Wing Body airlifter concept to validate the powered lift benefit and the low-speed handling characteristics. It has been shown that, due to its over-wing nacelle integration, the engine power setting has a major impact on the airframe aerodynamics [14].

In this thesis, two test facilities were built to investigate low-speed aerodynamic performance and validate some of the obtained numerical results. The first, comprised of a powered uninstalled nacelle, is described in section 4.1. The second test rig is a powered over-wing mounted nacelle configuration, which is described in Paper E, along with the major results of the experimental campaign.

# Chapter 3

## Methods

This chapter describes all the methods developed and utilized in this thesis. The methods were implemented in an integrated engine/aircraft integration aerodynamic design framework, which has been used to carry out the analysis presented in the attached paper.

### 3.1 Geometry Generation

#### 3.1.1 Class Shape Transformation Method

Class Shape Transformation (CST) curves were used to generate the nacelle geometries presented in this work. The CST method [85], [86] consists of a robust and versatile approach for the parametric representation of aerodynamic shapes, which allows the construction of smooth and complex geometries with few design variables. A CST shape can be mathematically represented by the product of a class function  $C(\psi)$  and a shape function  $S(\psi)$ , as follows:

$$\xi(\psi) = S(\psi) C(\psi) + \psi \Delta \xi_{te} \quad (3.1)$$

where  $\xi = r/c$ ,  $\psi = x/c$ , and the term  $\psi \Delta \xi_{te}$  modifies the trailing edge's radial coordinate. The class function, which determines the basic profile, is defined as:

$$C(\psi) = \psi^{N_1} (1 - \psi)^{N_2} \quad (3.2)$$

The exponents  $N_1$  and  $N_2$  in Eq. (3.2) are used to define the class of the geometric shape. For a round nose and a sharp trailing edge,  $N_1 = 0.5$  and  $N_2 = 1$ . The shape function is used to transform the class function and can be represented by an  $n$ th-order Bernstein polynomial, defined as

$$BP_n(\psi) = \sum_{i=0}^n \left[ K_{i,n} \cdot \left( \psi^i (1 - \psi)^{n-i} \right) \right] \quad (3.3)$$

where  $K_{i,n}$  are the binomial coefficients, which can be written as:

$$K_{i,n} = \frac{n!}{i!(n-i)!} \quad (3.4)$$

The shape function final form is obtained by multiplying Eq.(3.3) by weighting coefficients,  $bp_i$

$$S(\psi) = \sum_{i=0}^n [bp_i \cdot K_{i,n} \cdot (\psi^i (1 - \psi)^{n-i})] \quad (3.5)$$

and thus the CST function final form becomes:

$$\xi(\psi) = \sum_{i=0}^n [bp_i \cdot K_{i,n} \cdot (\psi^i (1 - \psi)^{n-i})] C(\psi) + \psi \Delta \xi_{te} \quad (3.6)$$

The first weighting coefficient,  $bp_0$ , is directly related to the highlight radius of curvature,  $R_{le}$ , by the relation:

$$bp_0 = \sqrt{\frac{2R_{le}}{c}} \quad (3.7)$$

The last weighting coefficient,  $bp_n$ , is related to the boattail angle added to a term that modifies the trailing edge's radial coordinate, as follows:

$$bp_n = \tan(\beta_{te}) + \frac{\Delta \xi_{te}}{c} \quad (3.8)$$

To calculate the remaining weighting coefficients and hence to fully determine  $\xi(\psi)$ , a set of constraints must be defined, which can be either control points or derivatives. Once these constraints are specified, a  $(n - 1)$  by  $(n - 1)$  linear set of equations  $\mathbf{A} \cdot \mathbf{X} = \mathbf{B}$  is formed by rearranging Eq. (3.6) and its derivatives  $\xi(\psi)'$  and  $\xi(\psi)''$ . Where  $\mathbf{A}$  is the matrix of coefficients,  $\mathbf{B}$  is the matrix on constant terms, and  $\mathbf{X}$  is the matrix of weighting coefficients, as follows:

$$\mathbf{A} = \begin{bmatrix} a_{1,1} & a_{1,2} & \cdots & a_{1,n} \\ a_{2,1} & a_{2,2} & \cdots & a_{2,n} \\ \vdots & \vdots & \ddots & \vdots \\ a_{n-1,1} & a_{n-1,2} & \cdots & a_{n-1,n-1} \end{bmatrix} \quad (3.9)$$

$$\mathbf{B} = \begin{bmatrix} b_1 & b_1 & \cdots & b_{n-1} \end{bmatrix}^T \quad (3.10)$$

$$\mathbf{X} = \begin{bmatrix} bp_1 & bp_1 & \cdots & bp_{n-1} \end{bmatrix}^T \quad (3.11)$$

### 3.1.2 Nacelle Parametrization

A 2D nacelle geometry is fully defined by joining six different CST curves, representing the inlet, fan cowl, bypass and core nozzle outer parts, core cowl, core nozzle, and plug. This section provides a brief description of how the CST curves are parametrized to generate a full nacelle shape. The main parameters for the inlet and fan cowl geometric representation are depicted in Fig. 3.1 and the input parameters for the cowl and inlet are described in Table 3.1.

A 4th-order Bernstein polynomial defines the fan cowl. As mentioned previously,  $R_{le}$  and  $\beta_{te}$  are set as inputs to calculate the first and last weighting coefficients

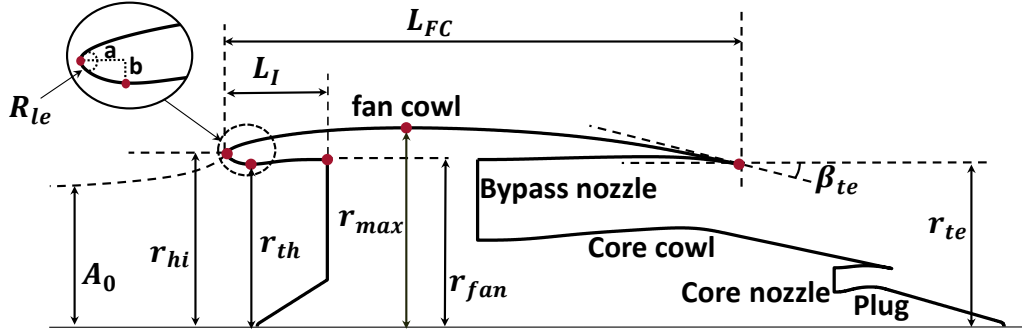


Figure 3.1: Fan cowl and inlet main geometric parameters.

Table 3.1: Fan cowl and inlet design parameters

Parameter	Description
$L_I/D_{fan}$	Inlet length to fan diameter ratio
$r_{hi}^2/r_{th}^2$	Contraction ratio
$a/b$	Lip aspect ratio
$r_{hi}/r_{max}$	Highlight radius to maximum radius ratio
$r_{max}/r_{fan}$	Maximum radius to fan radius ratio
$f_{max} = x_{max}/L_{FC}$	Axial position of maximum diameter
$f_{le} = \frac{R_{le}f_{max}L_{FC}}{(r_{max}-r_{hi})^2}$	Non-dimensional leading-edge radius of curvature
$\beta_{te}$	Nacelle boattail angle
$\theta_d$	Inlet droop

directly. At the point of maximum radius,  $r_{max}$ , the first derivative is set to be zero and, at the trailing edge, the second derivative is the one to be constrained as zero. The inlet is defined similarly, with the only difference being that the first derivative is zero at its throat position. The class function coefficients  $N_1$  and  $N_2$  were set to be 0.5 and 1.0, respectively, for both the cowl and inlet. Figure 3.2 shows the constraints employed to the inlet and fan cowl.

Both the bypass and core nozzles are constructed by the union of two different CST curves, which define the nozzles' inner and outer parts. The main geometric parameters for representing the bypass nozzle are depicted in Figure 3.3. The parameterization of the core nozzle is analog to the bypass nozzle and thus will not be described here. The outer part of the bypass nozzle is defined by a 6th-order Bernstein polynomial, whilst a 7-th order function represents its inner part (core cowl).

As can be seen in Fig. 3.4, the first and second derivatives are constrained to zero at the beginning of the outer and inner nozzle curves. Furthermore, the second derivative is zero at the end of the CST curves, and a given boattail angle determines the first derivative. For the core cowl, the first derivative is set as zero at the point

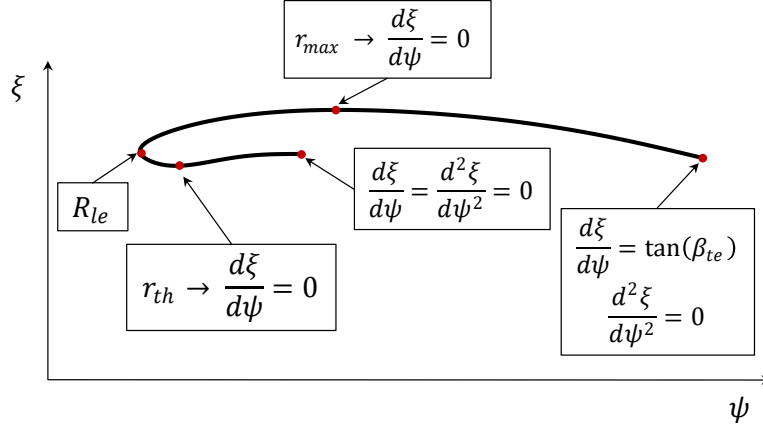


Figure 3.2: Constraints definition for the inlet and fan cowl. The control points are highlighted in red.

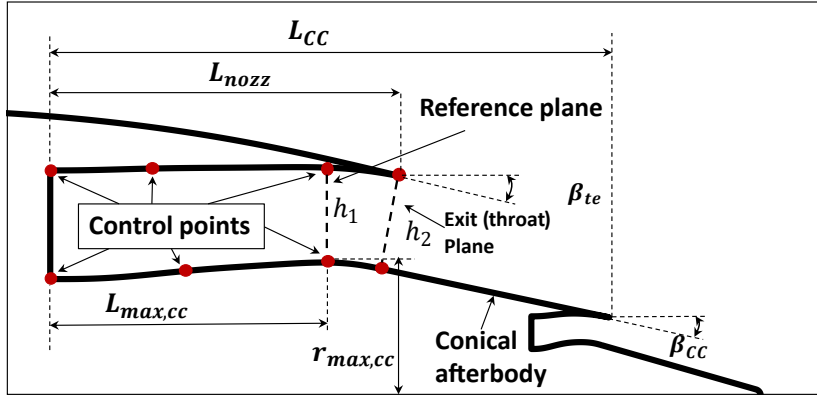


Figure 3.3: Bypass nozzle main geometric parameters.

of maximum radius  $r_{max,cc}$ . The class function coefficients were chosen to be  $N_1 = 0$  and  $N_2 = 1$  for both the inner and outer parts of the nozzles. The main input design parameters for the bypass nozzle are described in Table 3.2.

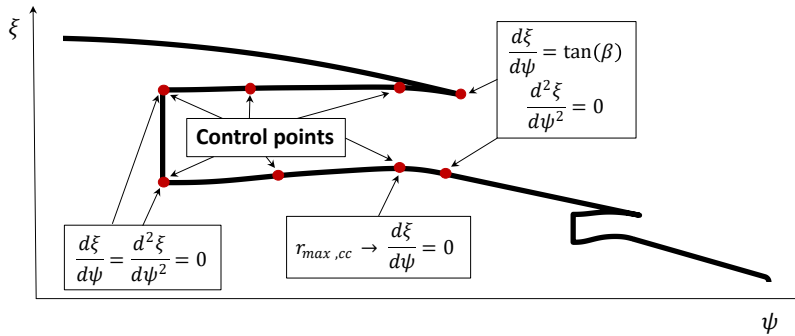


Figure 3.4: Constraints definition for the bypass nozzle.

Table 3.2: Bypass nozzle main design parameters

Parameter	Description
$L_{nozz}/D_{fan}$	Bypass duct length to fan diameter ratio
$h_1/h_2$	Nozzle area ratio
$r_{max,cc}/r_{fan}$	Maximum core cowl radius to fan diameter ratio
$\beta_{cc}$	Core cowl trailing edge angle
$L_{cc}/D_{fan}$	Core cowl length to fan diameter ratio
$f_{max,cc}$	Axial position of maximum radius at the core cowl
$f_{cpx}$	Relative axial position of a given control point
$f_{cpr}$	Relative radial position of a given control point

### 3.1.3 3D Nacelle Geometry Generation

In order to create a full 3D nacelle shape, 2D parametrizations are performed for three different locations referred to as the crown, maximum half-breadth (MHB), and keel, at the 12, 3, and 6 o'clock positions, respectively, as shown in Fig. 3.5. The axial and radial coordinates are interpolated sinusoidally along the circumferential direction between the crown, MHB, and keel, to generate the right nacelle half. The left half is a mirror image of the left one.

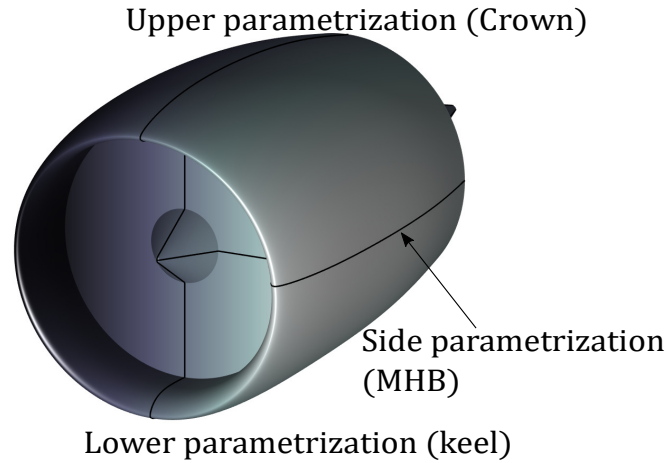


Figure 3.5: Nacelle 3D geometry definition.

The parametrization locations were selected to allow explicit geometric control where the local flow effects are expected to be critical. At the crown, the highest supersonic velocities are encountered and thus the strongest shocks are formed. Furthermore, the keel and MHB shapes play a fundamental role in preventing flow separation at high AoA and crosswind conditions.

Modern turbofan inlets are usually drooped for better alignment with the incoming flow, which is deflected upward due to the wing upwash [9], [87], [88]. A modification

was applied to the CST curves in order to droop the nacelle by a specified angle  $\theta_d$ . The drooping procedure is illustrated in Fig. 3.6 and described next. The crown and keel highlight positions are rotated around a pivoting point located at the intersection between the fan face plane and the engine centerline. A shape deformation function is then applied to the original CST curves so that the fan cowl and inlet are stretched to the new highlight position, proportionally to a quadratic function of the axial position.

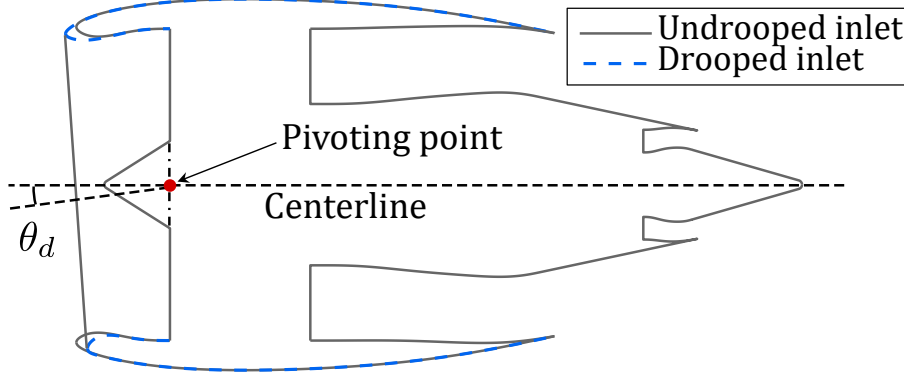


Figure 3.6: Drooped inlet representation.

Particularly for ultra-short inlets ( $L_I/D_{fan} < 0.4$ ), the internal lip curvature has shown to have a strong impact on flow separation when the nacelle was subjected to either high AoA or strong crosswinds. Therefore, to allow further control of the lip curvature, a control point was added between the highlight and the throat, for the keel and MHB positions.

### 3.1.4 Integration With the Aircraft

Installed configurations were studied in Papers A and B, where conventional UWN configurations are compared to advanced OWN mounts. The nacelle was integrated with the airframe by means of a pylon. The NASA wing-body Common Research Model (CRM), which is comprised of a modern supercritical wing and a fuselage, representative of a wide-body commercial aircraft [89], was used in this work. The pylon geometries were generated by vertically stacking NACA 4-digit airfoils.

The OWN mount usually requires a T-tail configuration, and therefore the conventional tail of the CRM was not included. The object of study of this work was a narrow-body aircraft, and thus the original CRM geometry was scaled down to the size of an A320, with respect to the reference chord (mean-aerodynamic chord),  $c_{ref}$ . The reference chord and area for the scaled aircraft are  $c_{ref} = 4.194 \text{ m}$ , and  $A_{ref} = 137.49 \text{ m}^2$ , respectively. The main engine angles and relative positions are illustrated in Fig. 3.7, for an OWN configuration.

### 3.1.5 Wing Reshaping

It has been discussed in section 2.2.2 that an over-wing mounted nacelle substantially disturbs the upper wing flow field and causes a significant lift reduction [79]. Although the lift can be easily recovered by increasing the aircraft AoA, the overall drag raises



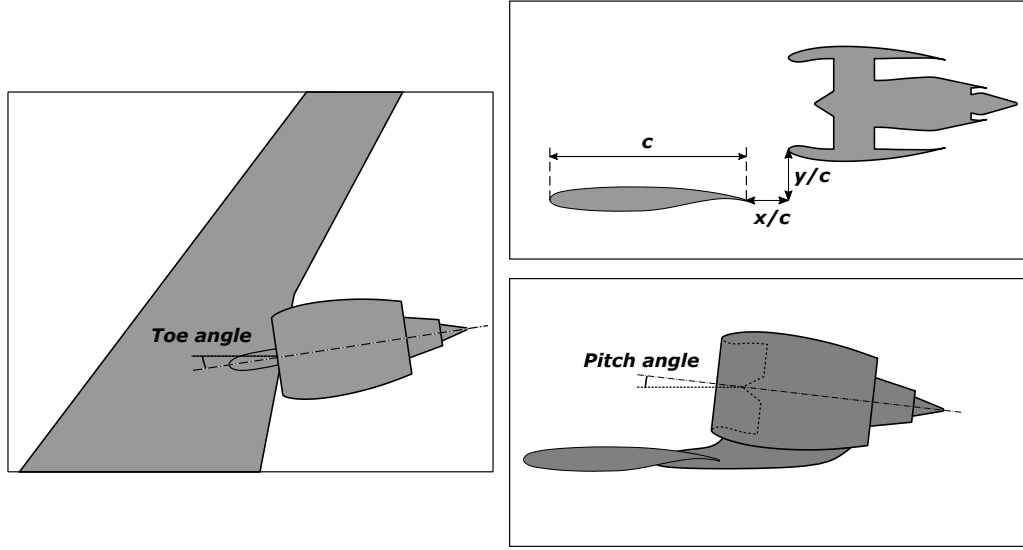


Figure 3.7: Wing-body-pylon-nacelle geometry schematic representation. The toe and pitch angles are highlighted, along with the definitions for the relative axial and vertical locations.

substantially, compared to a UWN configuration, mainly due to a stronger wing shock, and consequently higher wave drag. A way to improve the overall drag of the OWN configuration is to reshape the wing in the presence of the nacelle and pylon. In a first attempt, the wing was re-twisted locally, aiming to recover the sectional lift lost due to the engine installation. Although this method is able to unload the wing tip and reduce the wave drag at the outboard portion of the wing, a higher incidence is necessary at the inboard wing, especially in the pylon's vicinity, leading to a stronger shock and net increase in wave and overall drag.

To overcome this problem, a novel method for reshaping the original wing was developed. The method aims at recovering the spanwise lift distribution of the wing-body configuration without an increase in local incidence so that the strength of the wing shock is not raised considerably. Due to the high computational cost of the CFD simulations, it was decided that the number of wing design variables should be kept as low as possible. Therefore, the approach proposed here consists of jointly modifying the twist and camber at different wingspan locations by reshaping the original airfoils. This is accomplished by locally deforming the airfoil for a given trailing edge rotation,  $\theta_{te}$ . The deformation is performed by employing local rotations to the airfoil, proportional to a quadratic function of the axial position. The local rotation angle  $\theta(x/c)$  is calculated by the following expression:

$$\theta\left(\frac{x}{c}\right) = \theta_{te} \left(\frac{x}{c}\right)^2 \quad (3.12)$$

where  $x/c$  is the axial position normalized by the airfoil's chord. Figure 3.8a shows how the proposed method is able to maintain the local incidence,  $\alpha_i$ , unchanged whilst increasing the camber angle,  $\epsilon$ . Note that, because the trailing edge's position is being modified, the airfoil's twist will also not be the same. Figure 3.8b illustrates how the airfoil deformation is accomplished for  $\theta_{te} = 5^\circ$ . It can be seen that the

farther from the leading edge the axial position is, the more pronounced becomes the local rotation. Although this method has successfully been able to reduce shock strength, as shown in Paper D, the boattail angle is increased, potentially leading to a higher boattail drag due to a thicker boundary layer at the rear portion of the airfoil.

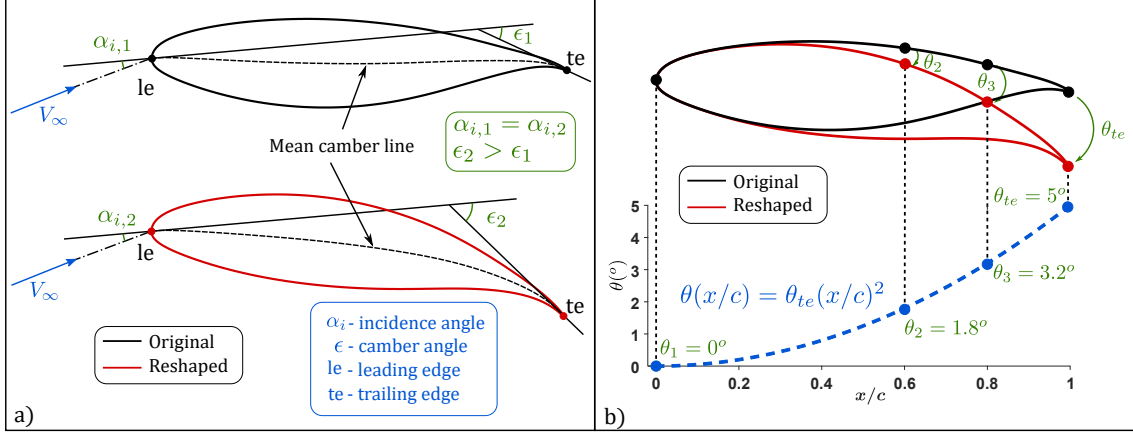


Figure 3.8: Airfoil deformation process: a) definition of incidence and camber angles, b) airfoil deformed proportionally to a quadratic function for  $\theta_{te} = 5^\circ$ .

The modified 3D wing is generated by reshaping the airfoils at the 8 spanwise sections shown in Fig. 3.9. The original airfoils are simultaneously modified iteratively until the desired sectional lift distribution is achieved.

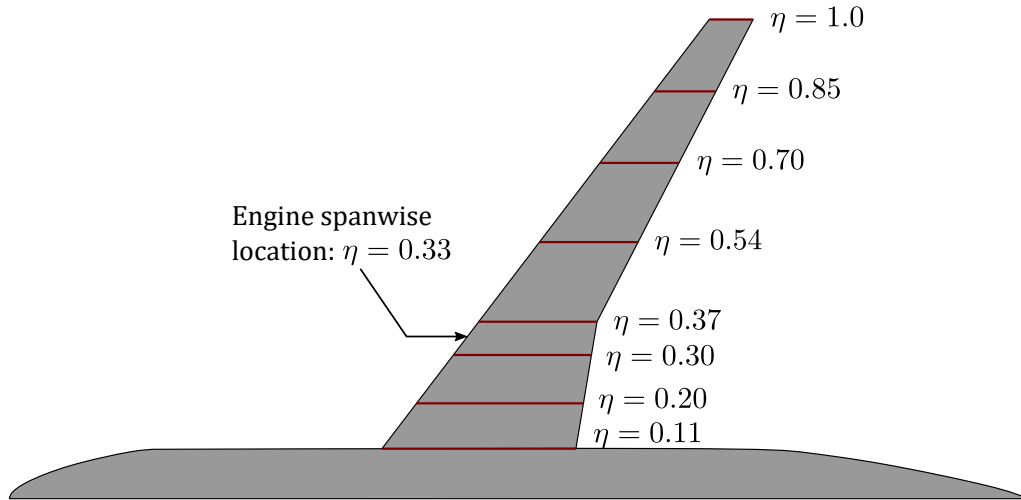


Figure 3.9: Spanwise location of the reshaped airfoils.

## 3.2 Numerical Approach

### 3.2.1 Standalone Nacelles

For the standalone nacelles, multiblock fully structured meshes were generated using the commercial software ANSYS ICEM CFD. The computational domain was defined

between the nacelle and a cylindrical far-field, with length and diameter equal to 50 times the fan diameter. The height of the wall adjacent cells was set so that  $y^+ < 1$ , for the cruise condition, in order to solve the viscous sub-layer. An example of 3D mesh for a standalone ultra-short nacelle is shown in Fig. 3.10.

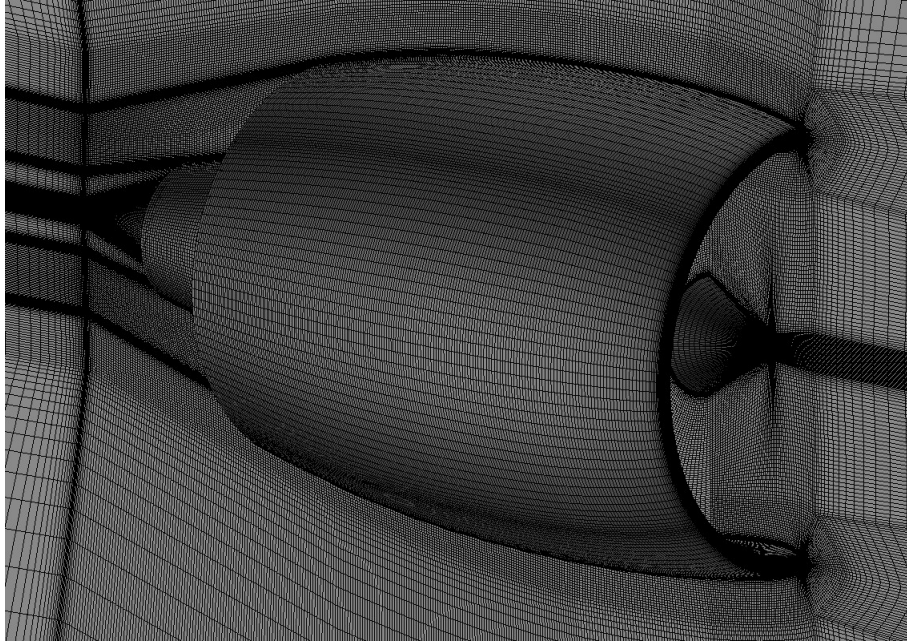


Figure 3.10: Multiblock structured 3D mesh for a standalone ultra-short nacelle.

The commercial software ANSYS FLUENT was used to perform the computational fluid dynamics (CFD) simulations and solve the flow field around the designed nacelle geometries. The computations were performed for the Reynolds-Averaged Navier-Stokes (RANS) equations, using the pressure-based solver, coupled with the  $k - \omega$  shear stress transport (SST) turbulence model. The pressure-velocity coupled algorithm was used. The least squares cell-based method was used for the computation of the flow field gradients and a second-order upwind scheme was employed to interpolate the convection terms along with the specific dissipation rate and the turbulent kinetic energy.

Figures 3.11a and 3.11b show a schematic representation of the CFD domain and boundary conditions (BC) employed for the 3D simulations. A pressure outlet BC was set at the fan face, where the static pressure profile was specified. Mass flow is targeted to assure mass flow continuity between the fan and nozzles. At the fan and low-pressure turbine outlets, mass flow inlet BCs were determined, where mass flow and total temperature were specified. For simulating crosswind operating conditions, the external far-field surface was split into two parts. One half was modeled using a pressure-inlet BC, where total pressure and total temperature are specified, whereas the other was set to be a pressure-outlet BC, where static pressure profile was specified (see Fig. 3.11b). For all the remaining cases a pressure farfield BC was used, where freestream static temperature, static pressure, Mach number, and flow direction were specified (see Fig. 3.11a). All the nacelle surfaces were defined as nonslip adiabatic walls. The spinner was treated as a rotating wall.

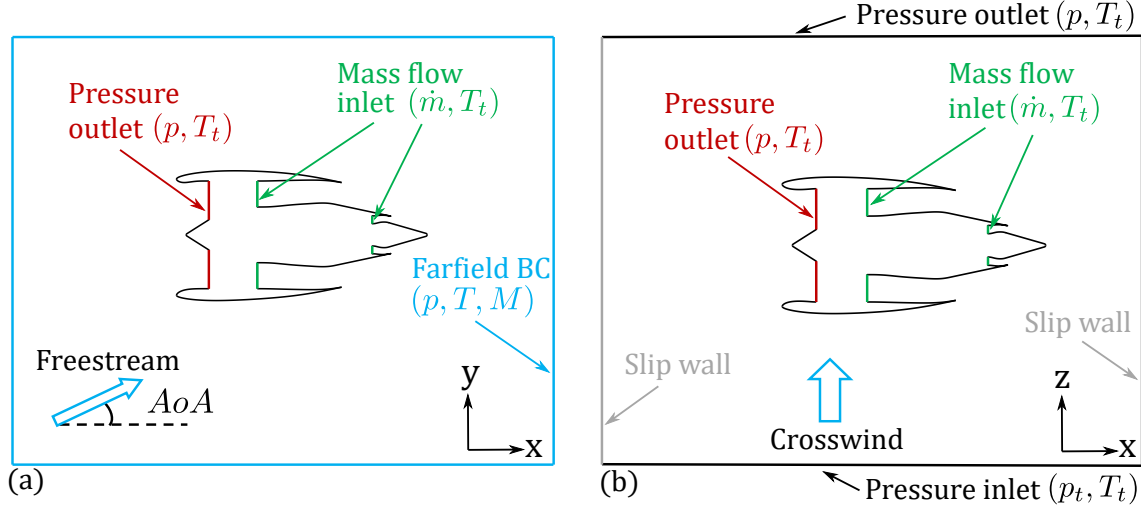


Figure 3.11: Boundary conditions and CFD domain schematic representation for the standalone nacelles cases for a) cruise and high AoA and b) crosswind.

### 3.2.2 Fan Face Boundary Condition

The initial stages of nacelle design require fast and reliable computations. Moreover, the aerodynamicist might not have access to the fan geometry. In such cases, simple and reliable boundary conditions are necessary to mimic the fan behavior and its coupling with the inlet. The modified parallel compressor method (MPC) has been developed to calculate the static pressure profile at the fan face and reproduce the fan behavior for highly distorted incoming flows. The method's intent is to be able to predict reasonably the fan's response to the incoming flow with a low amount of input data and low computational cost. The MPC method is an adaptation of the classical parallel compressor theory to CFD applications. This section provides a brief description of the parallel compressor theory followed by a detailed explanation of the developed MPC method.

The parallel compressor theory consists of a method to model the effects of inlet flow distortion on the engine stability and performance [60], [61], [90]. In its classical form, the compressor or fan is divided into two different sectors. Both discharge to the same static pressure, but with different total pressure and temperature. Therefore, to reach a uniform outlet static pressure, the spoiled compressor, with the lowest inlet total pressure, has to operate with a higher pressure ratio and vice-versa. In other words, the fan works harder in the regions of lower energy. Consequently, the lower the incoming total pressure, the lower the static pressure will be. Figure 3.12 illustrates the method in its simplest form. By applying the parallel compressor theory it is possible to predict compressor surge even if the mean operating point is far from the surge line.

The parallel compressor concept was adapted for CFD applications and used to compute the static pressure profile at the fan face, as described next. An imaginary discharge plane is defined downstream of the fan stator exit, where the flow is assumed to have uniform static pressure. The incoming flow field variables  $T_{1,i}$ ,  $p_{1,i}$ ,  $u_{1,i}$ ,  $w_{1,i}$ ,  $v_{1,i}$  and  $\dot{m}_i$ , together with the face area  $A_{1,i}$ , computed from the CFD

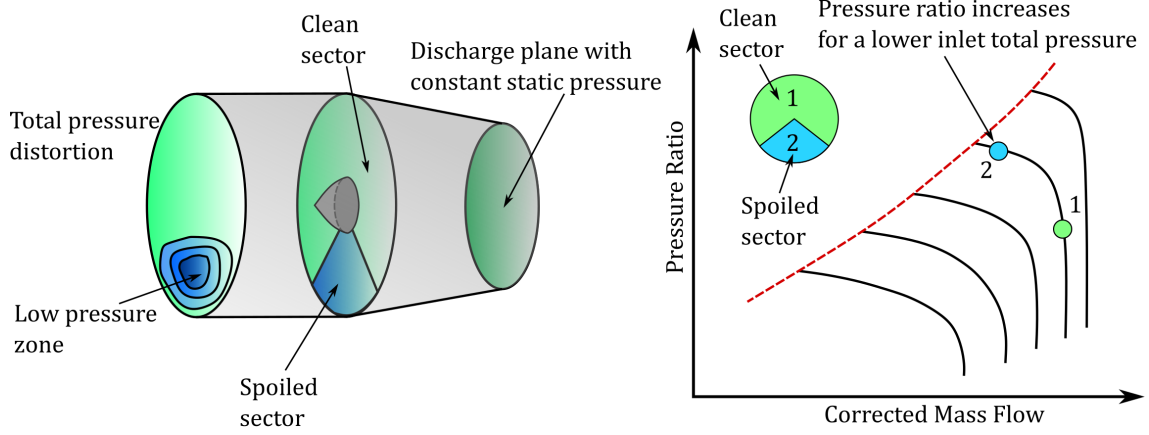


Figure 3.12: Schematic representation of the parallel compressor model. Adapted from [90].

iteration, are used to calculate the stagnation pressure  $p_{t1,i}$  and temperature  $T_{t1,i}$ , using Eq. (3.13) to Eq. (3.16), for a cell  $i$  at the fan face, as follows:

$$V_{1,i} = \sqrt{u_{1,i}^2 + v_{1,i}^2 + w_{1,i}^2} \quad (3.13)$$

$$M_{1,i} = \frac{V_{1,i}}{\sqrt{\gamma R T_{1,i}}} \quad (3.14)$$

$$p_{t1,i} = p_{1,i} \left( 1 + \frac{\gamma - 1}{2} M_{1,i}^2 \right)^{\frac{\gamma}{\gamma - 1}} \quad (3.15)$$

$$T_{t1,i} = T_{1,i} \left( 1 + \frac{\gamma - 1}{2} M_{1,i}^2 \right) \quad (3.16)$$

The corrected mass flux  $\phi_{corr,i}$  is calculated as

$$\phi_{corr,i} = \frac{\dot{m}_i \sqrt{T_{t1,i}/T_{t,ref}}}{A_{1,i} (p_{t1,i}/p_{t,ref})} \quad (3.17)$$

and a compressor speed line is used to obtain the local pressure ratio  $PR_i$  and isentropic efficiency  $\eta_{is,i}$ . The speed line is linearized around the engine operating point, for improved numerical stability. The stagnation pressure and temperature are computed at the imaginary outlet plane as

$$p_{t2,i} = p_{t1,i} PR_i \quad (3.18)$$

$$T_{t2,i} = T_{t1,i} + \frac{T_{t1,i}}{\eta_{is,i}} \left( PR_i^{\frac{\gamma-1}{\gamma}} - 1 \right) \quad (3.19)$$

so that the outlet Mach number and static pressure can be calculated, through Eq. (3.20) and Eq. (3.21), respectively.

$$\frac{\dot{m}_i \sqrt{R T_{t2,i}}}{p_{t2,i} A_{2,i}} = \sqrt{\gamma} M_{2,i} \left( 1 + \frac{\gamma - 1}{2} M_{2,i}^2 \right)^{\frac{\gamma+1}{2(\gamma-1)}} \quad (3.20)$$

$$p_{2,i} = \frac{p_{t2,i}}{\left(1 + \frac{\gamma-1}{2} M_{2,i}^2\right)^{\frac{\gamma}{\gamma-1}}} \quad (3.21)$$

The imaginary cell area  $A_{2,i}$  is obtained by assuming a constant area reduction ratio  $A_r$  between the fan entry and exit planes. Finally, the inlet static pressure is incremented by  $\Delta p$  until the outlet pressure  $p_{2,i}$  is equal to a target pressure  $p_{2,targ}$ . The pressure increment  $\Delta p$  can be calculated from Eq. (3.22), where  $\lambda$  is a weighting factor.

$$\Delta p = \lambda(p_{2,targ} - p_{2,i}) \quad (3.22)$$

Figure 3.13 shows a schematic representation of the stations and field variables used in the MPC method, whereas the calculation procedure is summarized in Fig. 3.14. The target pressure can be determined by using the thermodynamic properties obtained from the engine cycle calculations. Note that the only inputs necessary are:  $p_{2,targ}$ ,  $A_r$ , and the compressor or fan speed-line. The method is designed so that a generic map can be utilized and scaled to the engine's operating point.

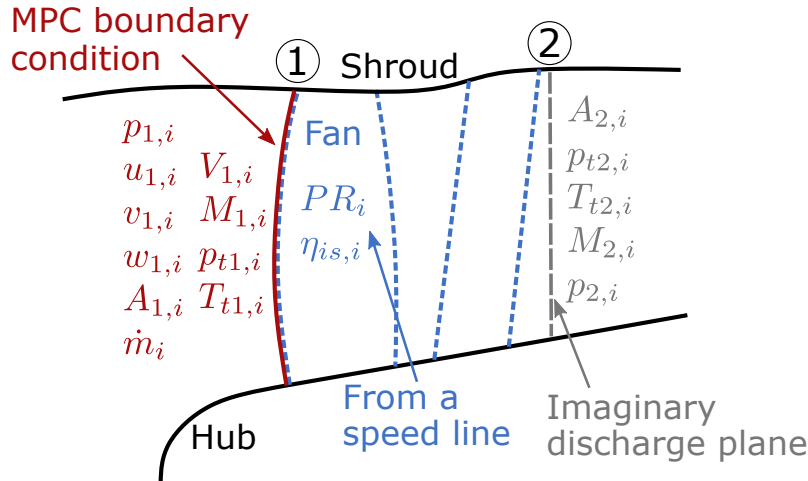


Figure 3.13: Schematic representation of the stations and field variables used in the MPC method. The subscript  $i$  refers to a certain cell at the fan face and its associated imaginary cell at the discharge plane.

The following assumptions are made in the derivation of the MPC method: 1) each mesh element at the fan face is acting as a parallel compressor and there is no circumferential flow migration between different parallel compressors. Consequently, the area reduction ratio between the inlet and outlet planes becomes the same for all the elements; 2) there is no blockage caused by secondary flows at the blade tip clearance; 3) the use of a single speed line assumes that the fan has the same behavior from the hub to the shroud. This approach captures variations in radial work caused by distorted flows, but is incapable of predicting variations in work caused by the fan blade geometry; 4) the fan is discharging to a constant outlet static pressure  $p_2$ . The impact of the underlined assumptions, as well as the MPC method limitations, will be further addressed in Paper A, where the method's validation is carried out.

Figure 3.15 shows an example of an application for the MPC method. On the left, the contours of normalized total pressure are shown, whilst the normalized static

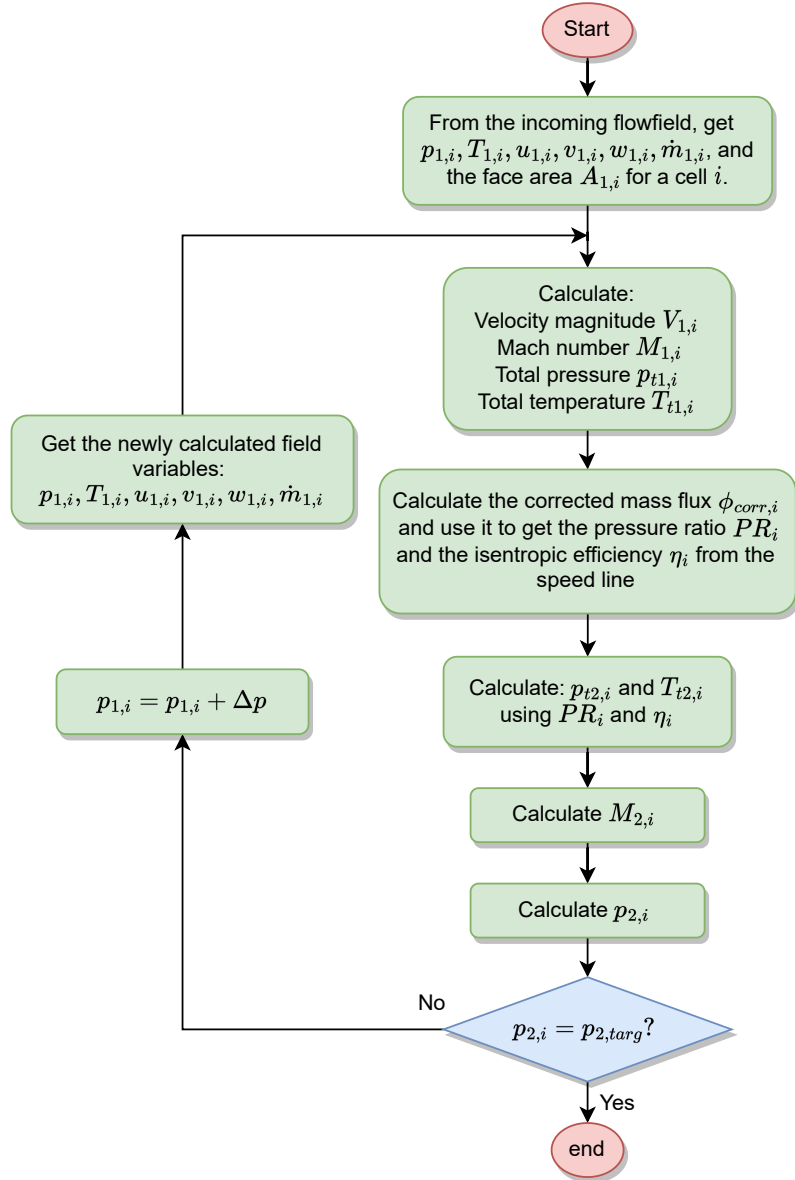


Figure 3.14: Flowchart of the modified parallel compressor method.

pressure is depicted on the right. The fan works harder in the low total pressure zone, decreasing the static pressure locally so that the exhaust pressure is uniform. Moreover, the MPC method reacts to the redistribution of momentum in the high total pressure zone, decreasing the static pressure in the locations where the mass flux increased.

### 3.2.3 Integrated Configurations

For the integrated configurations (wing-body-pylon nacelle), hybrid meshes were generated using the commercial software POINTWISE. The surface meshes, generated with the quad-dominant algorithm, are comprised of quadrilaterals and triangles. For the near wall elements, the T-Rex algorithm was used to create anisotropic tetrahedral,



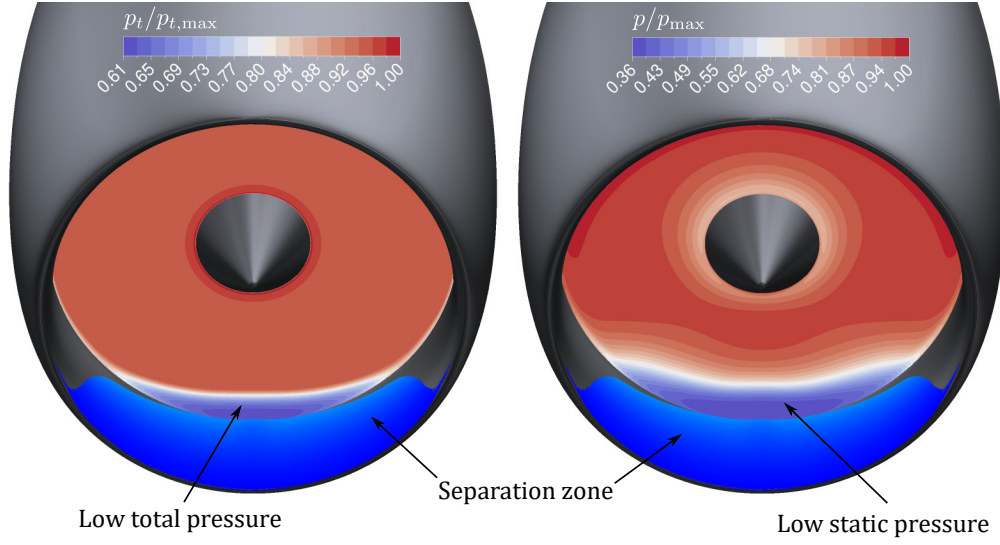


Figure 3.15: Example of the MPC method application. At the left are the contours of normalized total pressure and at the right are the contours of normalized static pressure.

hexahedral, prism, and pyramid elements, whereas the rest of the computational domain was populated with isotropic hexahedral layers with tetrahedral transitions, using the Voxel algorithm [91]. The computational domain is established between the half-span aircraft geometry, a half-sphere (farfield), and a symmetry plane. The farfield radius,  $R_{far}$  was defined as a hundred times larger than the reference chord  $c_{ref}$ , as recommended in the fourth AIAA drag prediction workshop (DPW-IV) guidelines [92]. The height of the wall-adjacent cells was set so that  $y^+ < 1$ , in order to properly resolve the viscous sub-layer. Figure 3.16 shows the surface and volume meshes used for an over-wing mounted nacelle configuration.

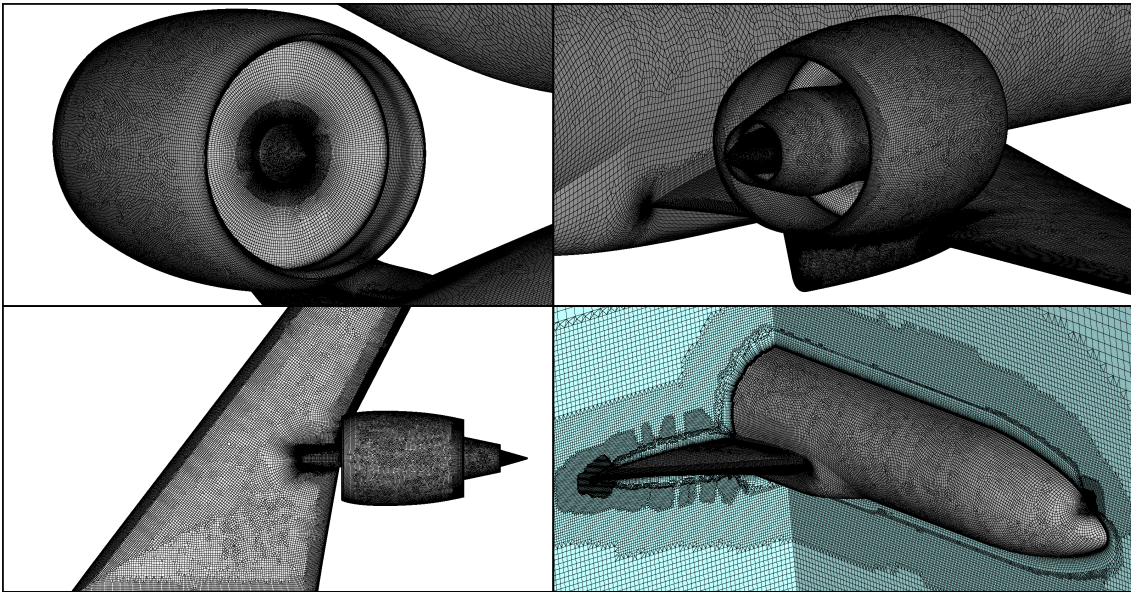


Figure 3.16: Surface and volume hybrid mesh for an OWN configuration.



The schematic representation of the computational domain and boundary conditions (BC) for the CFD simulations is depicted in Fig. 3.17. A pressure outlet BC is selected at the fan face, where the static pressure is iterated until a target mass flow is achieved. At the inlet of the core and bypass nozzles, a mass flow inlet BC was chosen, where mass flow and total temperature are specified. The external spherical domain is defined as a pressure far-field BC, where the Mach number, static pressure, and static temperature, and flow direction are specified. All the airframe and nacelle surfaces are set to be no-slip adiabatic walls. The spinner, in particular, is modeled as a rotating wall. The commercial software GASTURB was used to calculate the engine's thermodynamic cycle and define the boundary conditions. The engine cycle chosen in this work is aimed to be representative of a notional UHBPR turbofan engine. The freestream boundary conditions were selected for a typical narrow-body aircraft operating at cruise: a flight Mach number equal to 0.8 and an altitude of 35000 ft. The Reynolds number and reference temperature are respectively  $Re = 26.4$  million, and  $T_\infty = 218.81K$ .

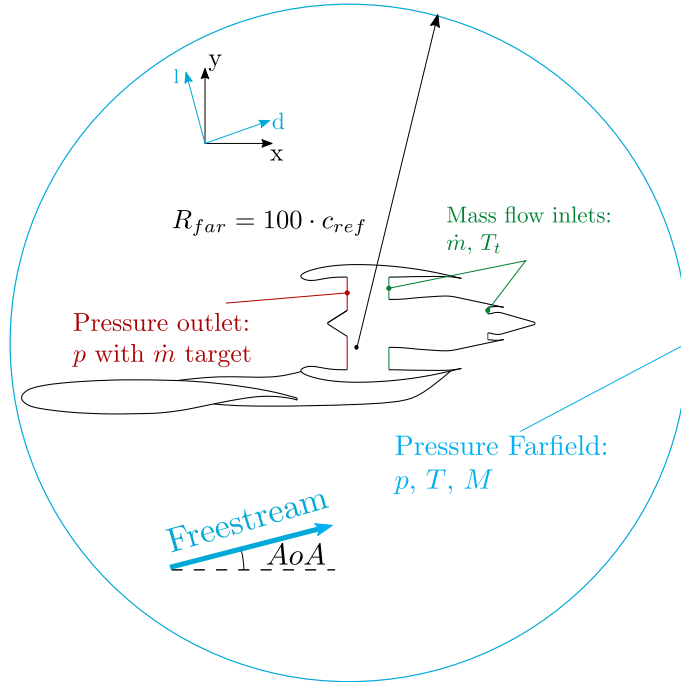


Figure 3.17: Schematic representation of the computational domain and boundary conditions for the integrated configurations.

### 3.3 Performance Metrics

#### 3.3.1 Thrust and Drag Bookkeeping

The thrust and drag bookkeeping formulation presented in Ref. [93] was used as the basis for the method presented in this work. Its derivation relies on integration over the nacelle and aircraft surfaces, and along the captured and post-exit streamtubes, and therefore it is considered a modified near-field bookkeeping method. Figure 3.18 shows a schematic representation of the forces acting on an over-wing mounted

two-stream nacelle configuration. The undisturbed flow is not always parallel to the aircraft's longitudinal axis, therefore, an aerodynamic frame of reference must be defined. In Fig. 3.18,  $x$  and  $y$  represent the aircraft reference frame, whilst  $l$  and  $d$  are the directions in which lift and drag are computed, respectively, where  $d$  is parallel to the free stream and  $l$  perpendicular to it.

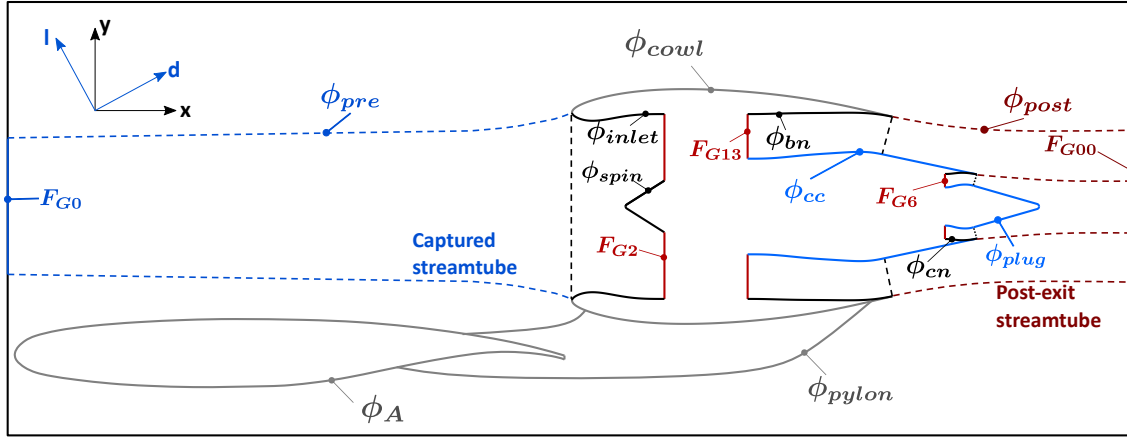


Figure 3.18: Forces acting on an over-wing mounted nacelle configuration, and definition of the aircraft and aerodynamic frames.

The forces acting on the nacelle, pylon, and aircraft wall surfaces, as well as on the captured and post-exit streamtubes' boundaries, can be expressed as follows:

$$\phi = \iint_S [(p - p_\infty) \mathbf{n} + \boldsymbol{\tau} \cdot \mathbf{n}] dS \cdot \mathbf{e}_d \quad (3.23)$$

where  $\mathbf{e}_d$  is the unit vector in the undisturbed flow direction. The stream gauge forces,  $F_G$ , can be defined as:

$$F_G = \iint_S [\rho \mathbf{V} (\mathbf{V} \cdot \mathbf{n}) + (p - p_\infty) \mathbf{n}] dS \cdot \mathbf{e}_d \quad (3.24)$$

The nacelle drag  $D_{nac}$  is defined as the integration of the viscous and pressure forces acting on the fan cowl,  $\phi_{cowl}$ , summed with the forces acting on the captured streamtube and exhaust plume, usually referred to as the pre-entry force,  $\phi_{pre}$ , and post-exit force,  $\phi_{post}$ , respectively [93], as follows:

$$D_{nac} = \phi_{pre} + \phi_{cowl} + \phi_{post} \quad (3.25)$$

One challenge in computing nacelle drag from CFD computations is the accurate prediction of  $\phi_{post}$ . Because the downstream force  $F_{G00}$  is unknown,  $\phi_{post}$  has to be computed by direct integration over the post-exit streamtube boundaries. However, for integrated configurations, the post-exit streamtube will present complex flow patterns, deviating significantly from an axisymmetric shape expected for standalone nacelles. The integration approach requires the exact geometry of the post-exit streamtube, as well as a considerable mesh refinement downstream of the nacelle, increasing significantly the computational cost of the simulations. For such reasons,

the computation of  $\phi_{post}$  is often avoided. A common practice is to define the modified nacelle drag  $D_{nac}^*$ , as follows:

$$D_{nac}^* = \phi_{pre} + \phi_{cowl} \quad (3.26)$$

Although  $D_{nac}^*$  has been used plenty of times [68], [70], [94], [95], it should be known that  $\phi_{post}$  is normally a forward force (thrust direction) which can have a significant magnitude, as shown in Ref. [70], and thus, neglecting such term can lead to an over-prediction of the nacelle drag.

The nacelle net propulsive force  $F_{net}^{NAC}$  can be calculated by applying the conservation of momentum to an enclosed control surface around the nacelle, which results in the definition presented in Eq. 3.27:

$$F_{net}^{NAC} = F_{G13} + F_{G6} - F_{G2} - (\phi_{bn} + \phi_{cc} + \phi_{cn} + \phi_{plug} + \phi_{cowl} + \phi_{spin} + \phi_{inlet}) \quad (3.27)$$

Different definitions thrust definitions can be used in bookkeeping methods [93]–[95]. The one employed in this thesis is referred to as the modified standard net thrust  $T_{net}^*$ :

$$T_{net}^* = F_{G13} + F_{G6} - F_{G0} - (\phi_{bn} + \phi_{cc} + \phi_{cn} + \phi_{plug}) \quad (3.28)$$

where the term “modified” refers to the inclusion of the plug and core cowl external forces in the original form of the standard net thrust. The pre-entry drag is obtained by employing the conservation of momentum to the captured streamtube:

$$\phi_{pre} = F_{G2} - F_{G0} + \phi_{spin} + \phi_{inlet} \quad (3.29)$$

By substituting Eq. 3.28 and Eq. 3.29 into Eq. 3.27,  $F_{net}^{NAC}$  becomes:

$$F_{net}^{NAC} = T_{net}^* - \phi_{pre} - \phi_{cowl} = T_{net}^* - D_{nac}^* \quad (3.30)$$

The aircraft net propulsive force,  $F_{net}$ , and the drag of the wing-body-pylon-nacelle (WBPN) configuration,  $D_{WBPN}$ , are defined by including the airframe and pylon forces,  $\phi_A$  and  $\phi_{pylon}$ , as follows:

$$F_{net} = T_{net}^* - \phi_{pre} - \phi_{cowl} - \phi_{pylon} - \phi_A = T_{net}^* - D_{nac}^* - \phi_{pylon} - \phi_A \quad (3.31)$$

$$D_{WBPN} = D_{nac}^* + \phi_{pylon} + \phi_A \quad (3.32)$$

The installation drag,  $D_{inst}$ , is calculated by subtracting the wing-body (WB) drag  $D_{WB}$  from  $D_{WBPN}$ , for the same lift, where  $D_{WB}$  is computed by integrating the pressure and viscous forces at the WB configuration’s surfaces (Eq. 3.23). The drag coefficient  $C_d$  can be defined by using the scaled CRM reference area  $A_{ref}$ , as follows:

$$C_d = \frac{D}{q_\infty A_{ref}} \quad (3.33)$$

where  $q_\infty$  is the dynamic pressure,  $0.5\rho_\infty V_\infty^2$ . Similarly, the lift coefficient,  $C_l$ , is expressed as:

$$C_l = \frac{L}{q_\infty A_{ref}} \quad (3.34)$$

### 3.3.2 Performance of Inlets and Nozzles

The performance of an inlet is usually described by the mass flow ratio MFR, total pressure distortion coefficient  $DC_{60}$ , and intake pressure recovery  $\eta_i$ . The MFR, consists of an aerodynamic reference parameter for the inlet and it is defined as the ratio of the streamtube captured area,  $A_0$ , and the highlight area,  $A_{hi}$ , as follows:

$$\text{MFR} = \frac{A_0}{A_{hi}} \quad (3.35)$$

The  $DC_{60}$  coefficient is a standard parameter used to assess the distortion level at the fan face, which can be defined as:

$$DC_{60} = \frac{\bar{p}_{t2} - \bar{p}_{t60}}{\bar{q}} \quad (3.36)$$

where  $\bar{p}_{t2}$  and  $\bar{q}$  are the area averaged total and dynamic pressures at the fan face, and  $\bar{p}_{t60}$  is the area averaged total pressure at the most distorted  $60^\circ$  circumferential sector at the fan face. The intake pressure recovery  $\pi_d$  is a measure of how much of the free-stream total pressure is retained after the flow passed through the inlet. It can be expressed as follows:

$$\pi_d = \frac{\bar{p}_{t2}}{p_{t\infty}} \quad (3.37)$$

where  $p_{t\infty}$  is the free-stream stagnation pressure.

The performance of the bypass and core nozzles can be expressed through the discharge and thrust coefficients, referred to as  $C_D$  and  $C_T$  respectively. The former is a measure of effective area reduction due to total pressure losses and blockage caused by boundary layer growth. The latter accounts for thrust losses due to non-isentropic phenomena such as the formation of shear layers between the freestream and the nozzle stream, shear stresses on the walls, and shock waves in choked nozzles.

The definitions used for the nozzle coefficients are in accordance with the formulation described in [96]. The discharge coefficient can be defined as the ratio between the actual mass flow to the ideal isentropic mass flow passing through the nozzle exhaust area  $A_{ex}$ . The ideal mass flow,  $\dot{m}_i$ , can be obtained from the isentropic relations for an ideal gas

$$\dot{m}_{id} = p_t A_{ex} \left(\frac{1}{\lambda}\right)^{\frac{1}{\gamma}} \sqrt{\frac{2\gamma}{(\gamma-1)RT_t} \left(1 - \left(\frac{1}{\lambda}\right)^{\frac{\gamma-1}{\gamma}}\right)} \quad (3.38)$$

where the nozzle pressure ratio,  $\lambda$ , is defined as

$$\lambda = \begin{cases} p_t/p_\infty, & \text{if } p_0/p_\infty < PR_{crit} \\ PR_{crit}, & \text{if } p_0/p_\infty \geq PR_{crit} \end{cases} \quad (3.39)$$

and the critical pressure ratio,  $PR_{crit}$ , as

$$PR_{crit} = \left( \frac{\gamma + 1}{2} \right)^{\frac{\gamma}{\gamma-1}} \quad (3.40)$$

The core and bypass discharge coefficients can then be respectively written as

$$C_{D_{cn}} = \frac{\dot{m}_{cn}}{\dot{m}_{id,cn}} \quad (3.41)$$

$$C_{D_{bn}} = \frac{\dot{m}_{bn}}{\dot{m}_{id,bn}} \quad (3.42)$$

where  $\dot{m}_{cn}$  and  $\dot{m}_{bn}$  are the actual mass flows of the core and bypass nozzles.

The overall thrust coefficient is given by the ratio of the actual gross thrust  $T_{gross}$  and the sum of the ideal core and bypass nozzle thrusts. The ideal thrust is defined as the product of the actual mass flow and the ideal velocity  $V_{id}$ , resulting from an isentropic expansion to the ambient pressure. The ideal isentropic velocity,  $V_{id}$ , is defined as:

$$V_{id} = \sqrt{\frac{2\gamma RT_t}{(\gamma-1)} \left( 1 - \left( \frac{1}{p_t/p_\infty} \right)^{\frac{\gamma-1}{\gamma}} \right)} \quad (3.43)$$

and hence  $C_T$  can be expressed as:

$$C_T = \frac{T_{gross}}{\dot{m}_{bn} V_{id,bn} + \dot{m}_{cn} V_{id,cn}} \quad (3.44)$$

where  $T_{gross}$  is the gross thrust produced by the nozzles.

### 3.4 Nacelle Design Process

The methods described above were coupled together to form an integrated aerodynamic design framework, comprised of engine cycle calculations, parametric nacelle shape definition, automatic structured multi-block mesh generation, 3D RANS CFD computations, and aerodynamic performance evaluation. Figure 3.19 presents the flowchart of the overall nacelle design procedure, which can be applied for both conventional-length and ultra-short nacelles.

Initially, all the operating conditions to be considered in the nacelle design process should be defined, and the respective design and off-design cycle calculations carried out. The commercial software GASTURB was used to conduct the engine performance calculations. The design-point data, along with the geometric input data is used to shape the nacelle using the CST method (see section 3.1.1). The 3D nacelle design starts from a 2D-axisymmetric geometry. In this work, the baseline geometry was obtained by means of 2D-axisymmetric CFD simulations and parametric studies. After the geometry is defined, the multiblock structured mesh is automatically generated and the 3D RANS CFD computations are performed. The cycle data associated with the operating condition are used to define the boundary conditions, together with the MPC method, described in section 3.2.2. The nacelle's aerodynamic

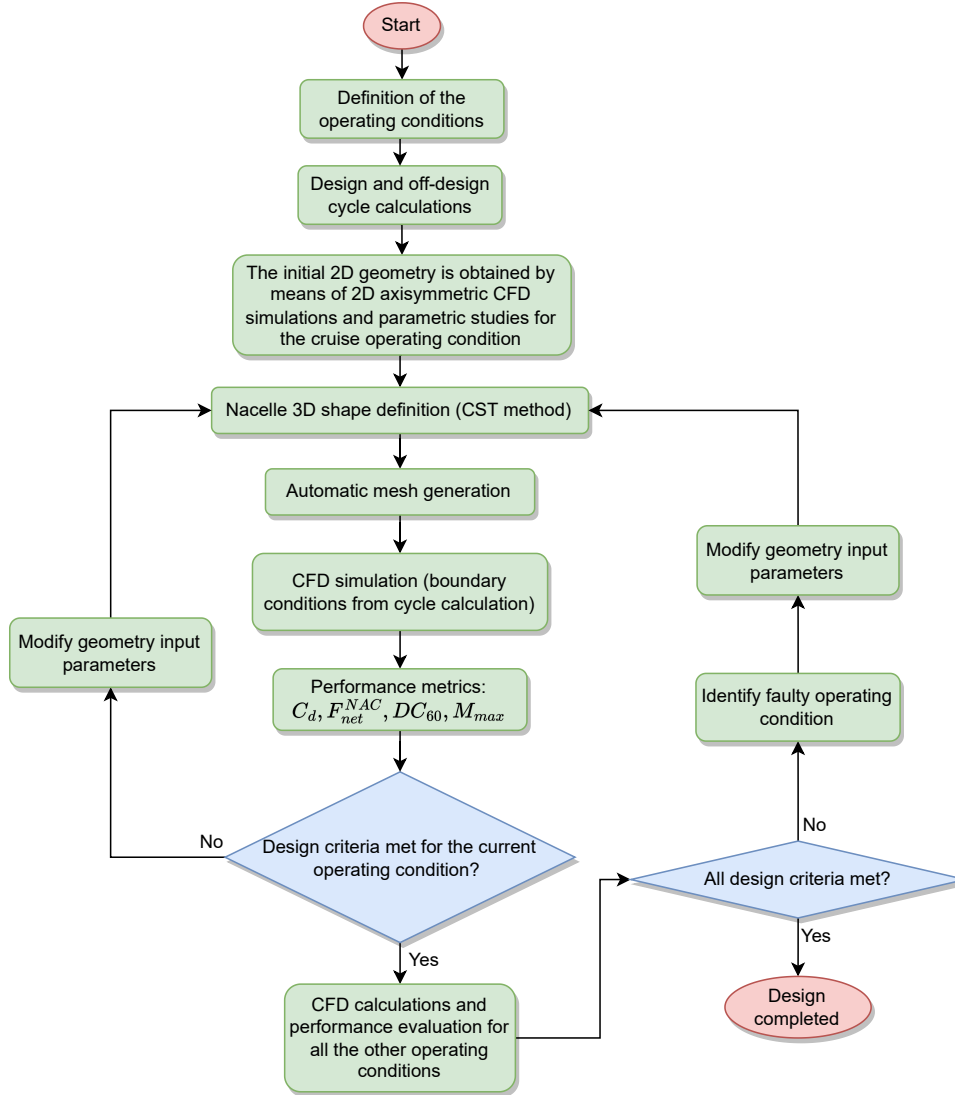


Figure 3.19: Flowchart of the design procedure.

performance is evaluated by bookkeeping of thrust and drag (see section 3.3.1), plus the performance metrics described in section 3.3.2. In case the established design criteria are not met for a specific operating condition, new geometric input parameters are defined and the process is reiterated until the desired performance is achieved. Afterward, CFD simulations are performed for all the remaining operating conditions. In case the design criteria are not met for some operating condition, the geometry is modified and the process is reiterated, initially for the faulty operating point, and lastly for the remaining operating conditions. The design process finishes only when all the criteria are met for all the operating conditions.

This process can be laborious and time demanding, especially due to the high computational time necessary to fulfill all the steps. It is therefore of paramount importance for the designer to have a deep understanding of the flow field behavior and of which parameters play a major role in the nacelle's aerodynamic performance so that the number of iterations can be minimized.

### 3.4.1 Operating Conditions

In the early design stage, it is not practical to consider all the segments existent in the aircraft mission, due to the high computational costs of the 3D CFD simulations. Therefore, only operating conditions considered to be critical were used in this thesis. The operating conditions shown in Table 3.3, obtained from [30], were used for fulfilling the suggested design approach. The next paragraph provides a discussion about the motivations behind the choice of operating conditions.

Table 3.3: Operating conditions for the design of nacelles

Condition	$M_\infty$	Altitude (m)	AoA ( $^\circ$ )
Cruise	0.8	10668	5
Wing $C_{l_{max}}$	0.25	4267.2	29
Take-off rotation	0.25	0	17
Crosswind	0.0442	0	0

At cruise, the main goal is to minimize drag, therefore shock waves should be avoided when possible and the maximum Mach number should be limited. The engine is usually subjected to a local AoA of approximately  $5^\circ$ , caused by a combination of the wing up-wash and the aircraft AoA. The wing maximum lift coefficient  $C_{l_{max}}$  condition, represents a near stall operating point, in which the aircraft is subjected to the highest AoA allowed in flight. Although not typically encountered in the flight mission, the  $C_{l_{max}}$  condition plays an important role in the certification procedure [30]. In this case, the main concerns are internal inlet separation and distortion levels at the fan face. The take-off (TO) rotation condition occurs at the end-of-runway when the aircraft nose is pitching up. Inlet separation and high distortion are also major problems since the engine is subjected to relatively high incidence. Aircraft certification requires safe and stable operation at takeoff and landing under  $90^\circ$  crosswinds, for a wind velocity of at least 20 knots [97]. When subjected to crosswind, inlet flow separation can occur, leading to high levels of distortion and possibly to fan surging. Therefore, crosswind components should be considered during the nacelle design procedure.

## 3.5 Aircraft Equilibrium of Forces

To compare the aerodynamic performance of different aircraft configurations, it is desirable that all the forces are balanced. Therefore, not only  $C_l$  has to be the same, but also  $F_{net} = 0$  should be zero. The flowchart with the procedure to simultaneously obtain the target  $C_l$  and  $F_{net} = 0$  is shown in Fig. 3.20. The initial boundary conditions are defined based on the cycle data for an estimated net thrust. A CFD calculation is conducted for a guessed AoA and  $C_l$  is computed. The AoA is iterated until  $C_l$  reaches its target value. Subsequently, the mass flow at the fan face  $\dot{m}_f$  is iterated until  $F_{net} = 0$ , for the same BPR. For every change in  $\dot{m}_f$ ,  $C_l$  is re-iterated. This method was used in Papers C and D, where the target  $C_l$  was 0.5, the same as the CRM's.

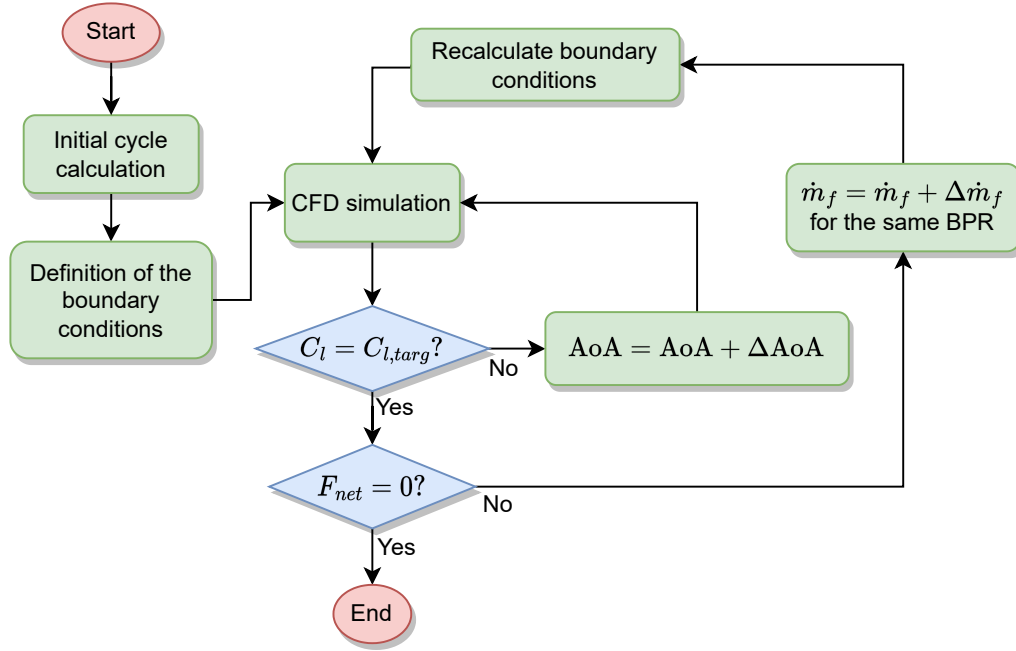


Figure 3.20: Flowchart of the procedure to obtain  $F_{net} = 0$ .

As mentioned earlier, the CRM tails were not included in any of the studied configurations. However, by neglecting the tail drag, the engine throttle condition for  $F_{net} = 0$ , would be underestimated. Therefore, the tail drag was estimated by using Raymer's drag component buildup method [98].



# Chapter 4

## Experimental Investigation

Two test rigs have been developed to investigate the low-speed behavior of powered standalone and installed nacelles. The first rig is comprised of an 8.6% scale standalone nacelle powered by the Schubeler DS-215-DIA electric ducted fan (EDF), whereas the second rig is a half-span, 5.3% scale, OWN configuration powered by a Schubeler DS-82-DIA EDF. For the standalone rig, both a general description and the main results of the test campaign are provided in this chapter. For the OWN rig, only a brief overview is given, since the detailed rig description and test results are available in Paper E.

### 4.1 Test Rig 1: Standalone Nacelle

#### 4.1.1 Description

The first test rig was built to investigate the aerodynamic behavior of powered nacelles at low-speed conditions. An axisymmetric nacelle shape was mounted around the DS-215-DIA EDF so that the effects of inlet-fan coupling could be assessed. Figure 4.1 shows a schematic representation of the rig with its main parts. The parts comprising the outer part of the nacelle (lip, midbody, and afterbody) were assembled together and mounted on the top of two load cells, in order to measure the fan cowl force  $\phi_{cowl}$ . The remaining parts (inlet, nozzle, and core cowl) were connected to the EDF, which was attached to the strut through an u-shaped support. A 2 mm axial gap was necessary to allow the outer nacelle assembly to move in the engine's centerline direction so that the inner lip would not touch the inlet and interfere with the load cells' measurements. The split between the inlet and lip was performed to guarantee flexibility for geometry replacement so that different shapes could be tested without the need to modify the rear part of the nacelle.

The assembled rig is shown in Fig. 4.2. The rig was mounted on the top of a rotary table so that the nacelle could be rotated around the vertical axis, allowing AoA variation. The inlet, lip, core cowl, and fairing were 3D printed in plastic, whilst the remaining parts were made out of aluminum.

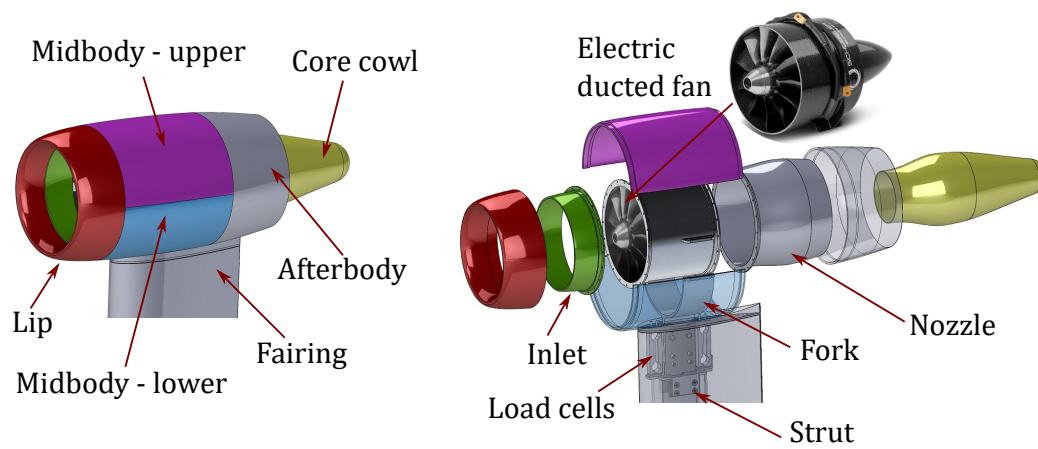


Figure 4.1: Schematic representation of the standalone nacelle rig.

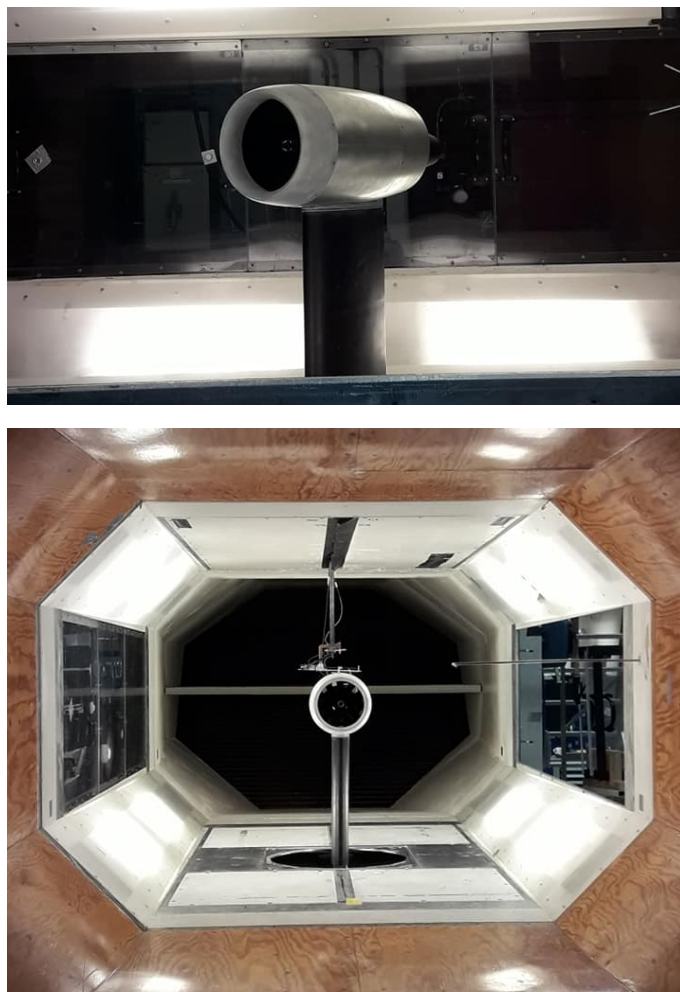


Figure 4.2: Nacelle rig mounted in the wind tunnel.

### 4.1.2 Results

The wind tunnel tests were carried out for different AoAs, freestream velocities  $V_\infty$ , and fan rotational speeds. A wind tunnel mapping was carried out, where the AoA was varied from  $0^\circ$  to  $20^\circ$  and  $V_\infty$  ranged from 10 to 50 m/s. The fan power request was kept constant and thus the rotational speed varied slightly for different cases. The average rotational speed was equal to 7817 rpm. The Reynolds number ranged from  $2.96 \times 10^5$  to  $1.48 \times 10^6$ .

The results obtained from the load cells' measurements are depicted in Figure 4.3. Note that the force measured here cannot be called drag, because it includes a 'potential flow buoyancy' term, which is the integrated pressure force in potential flow [93]. It can be observed that  $\phi_{cowl}$  is sometimes negative (points forward) for low  $V_\infty$ . This occurs due to a well-known phenomenon often referred to as lip thrust. Due to the convex shape, the flow accelerates around the lip and creates a low-pressure region both externally and internally (near the throat). This suction zone creates a negative (forward) forebody force, which seems to be predominant at low speeds. At higher speeds, the lip suction effect is outweighed by the nacelle pressure and viscous drag, and the resultant force becomes positive. An unexpected behavior was encountered for the  $V_\infty = 50$  m/s case. It is believed that the cables which power the fan might have touched the inner fan cowling surface, interfering with the load cell measurements.

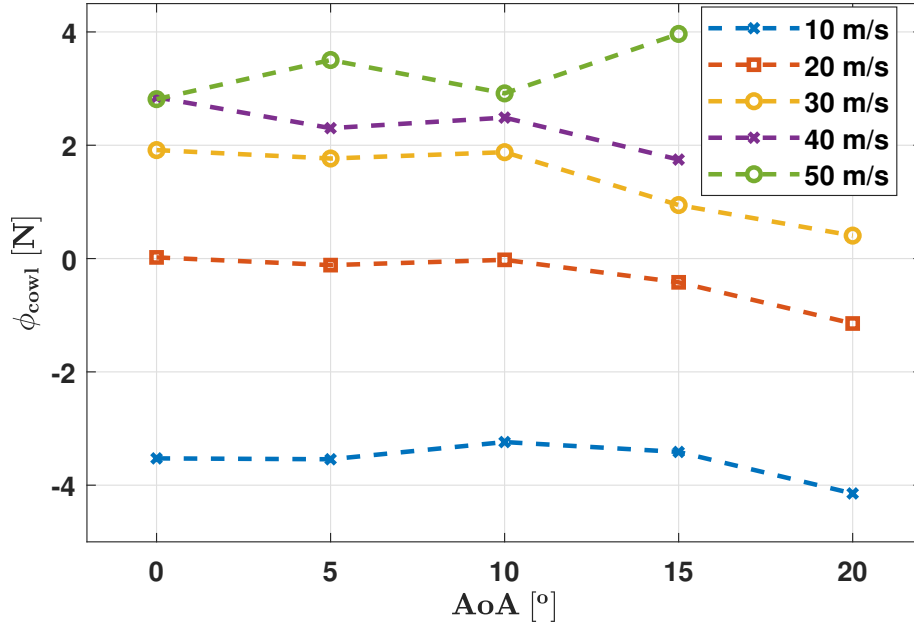


Figure 4.3: Fan cowling force versus angle of attack for different wind tunnel speeds. The fan power request was set as 80% of the maximum power.

A second set of measurements was obtained by varying the fan power setting for a constant AoA and  $V_\infty$ . Figure 4.4 shows the fan rotational speed,  $N$ , plotted against  $\phi_{cowl}$  for AoA =  $0^\circ$ ,  $V_\infty = 10$  m/s, where the input request varied from 40 to

100% of the maximum power. It can be observed that the measured force increases with  $N$ , which is likely caused by an increased pre-entry force  $\phi_{pre}$ , due to a higher captured stream-tube momentum flux.

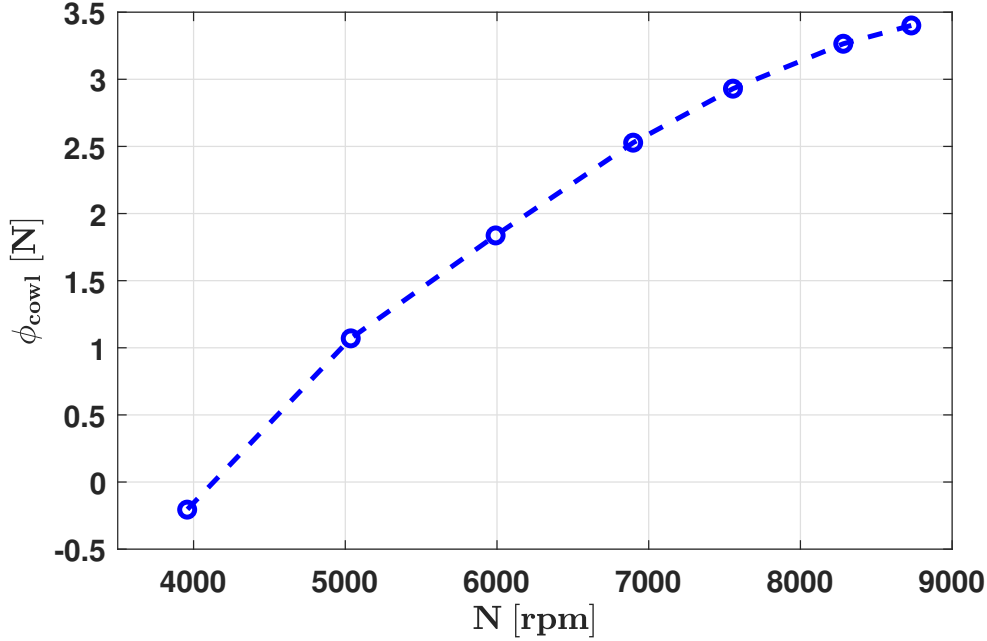


Figure 4.4: Variation of  $\phi_{cowl}$  with the EDF rotational speed for  $AoA = 0^\circ$ ,  $V_\infty = 10$  m/s.

To assess the influence of the fan throttle on the nacelle flow field, surface tufts were placed on the leeward side of the fan cowl and on the windward side of the internal lip, where separation is more likely to occur. Figure 4.5 shows the flow visualization results for  $AoA = 10^\circ$ , and  $V_\infty = 30$  m/s. In the top pictures, the fan was off, whilst in the bottom ones the fan rotational speed was equal to 7750 rpm. A separation bubble could be identified for the unpowered case, however, for the powered-on condition, the boundary layer was re-energized and the flow was reattached. This, not surprisingly, shows that the fan power setting has a major impact on the nacelle's internal and external flow, and justifies the construction of powered rigs rather than flow-through ones.

Although the standalone nacelle experimental investigation served as a valuable learning experience, some issues have led the testing campaign to be discontinued. Problems with the rig assembly such as cables touching the inner cowling surface, large gaps, and misalignments called the results into question. Moreover, since  $\phi_{pre}$  could not be measured, a proper bookkeeping of thrust and drag could not be accomplished. Nonetheless, the lessons learned from Rig 1 were valuable assets for the design and construction of Rig 2 (OWN configuration), which will be described in the section that follows.

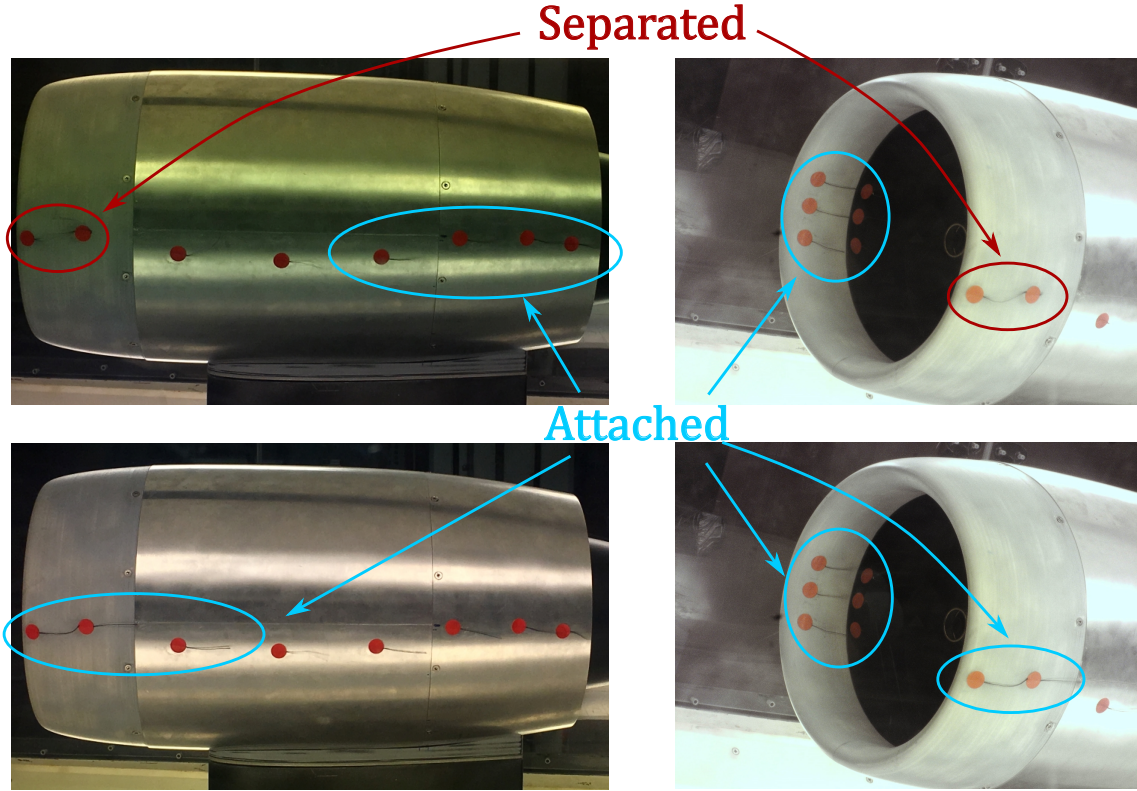


Figure 4.5: Flow visualization for  $AoA = 10^\circ$  and  $V_\infty = 30$  m/s. At the top are the results for the unpowered fan and at the bottom for  $N = 7750$  rpm. The surface tufts were attached to the leeward part of the fan cowl and to the windward part of the internal lip.

## 4.2 Test Rig 2: Over-wing Nacelle Configuration

A brief description of the installed powered test rig is provided in this section, along with a discussion of the main phenomenon studied. Paper E provides a detailed rig description and the major results of the test campaign. The configuration choice for the installed nacelle tests is a half-span, 5.3% scale, OWN mount, following the results obtained in Papers C and D, where the potential benefits of such integration choice are discussed thoroughly. In this test campaign, the aim is to investigate a unique characteristic of OWN installations, which is the powered lift benefit at low-speed operating conditions. As mentioned in section 2.2.2, at low speeds, the engine operates at a high power setting ( $MFR > 1$ ), which creates a low-pressure zone upstream of the engine. For engines mounted over the wings, this low-pressure region reduces the pressure at the wing's upper surface and creates an overall lift benefit (see Fig. 2.6).

Similarity with real flight operating conditions cannot be achieved in the Chalmers low-speed wind tunnel, which operates at an order of magnitude lower  $Re$ . However, freestream Mach numbers,  $M_\infty$ , up to 0.18 can be achieved, which can be representative of takeoff speeds. Nevertheless, the experimental campaign aimed to capture the impact of the momentum variation upstream of the engine on the wing lift and pressure distribution. This depends mostly on the engine power setting, which will



be proportional to the MFR. The experiments are compared to CFD simulations in Paper E for the same wind tunnel conditions and including the wind tunnel walls.

The over-wing nacelle model mounted in the wind tunnel is shown in Fig. 4.6. It is comprised of the following parts: wing, test section, fuselage, nacelle lower part, nacelle upper part, and plug. The test section features a total of 66 channels for surface pressure measurements. A six-component load cell was attached to the wing root and fuselage center for lift measurements. The nacelle, which is attached to the wing through a pylon, can be removed so that measurements can be conducted for the clean airframe (wing-body) configuration. Furthermore, the model is powered by a 120 mm EDF and has a half-span of 930 mm.

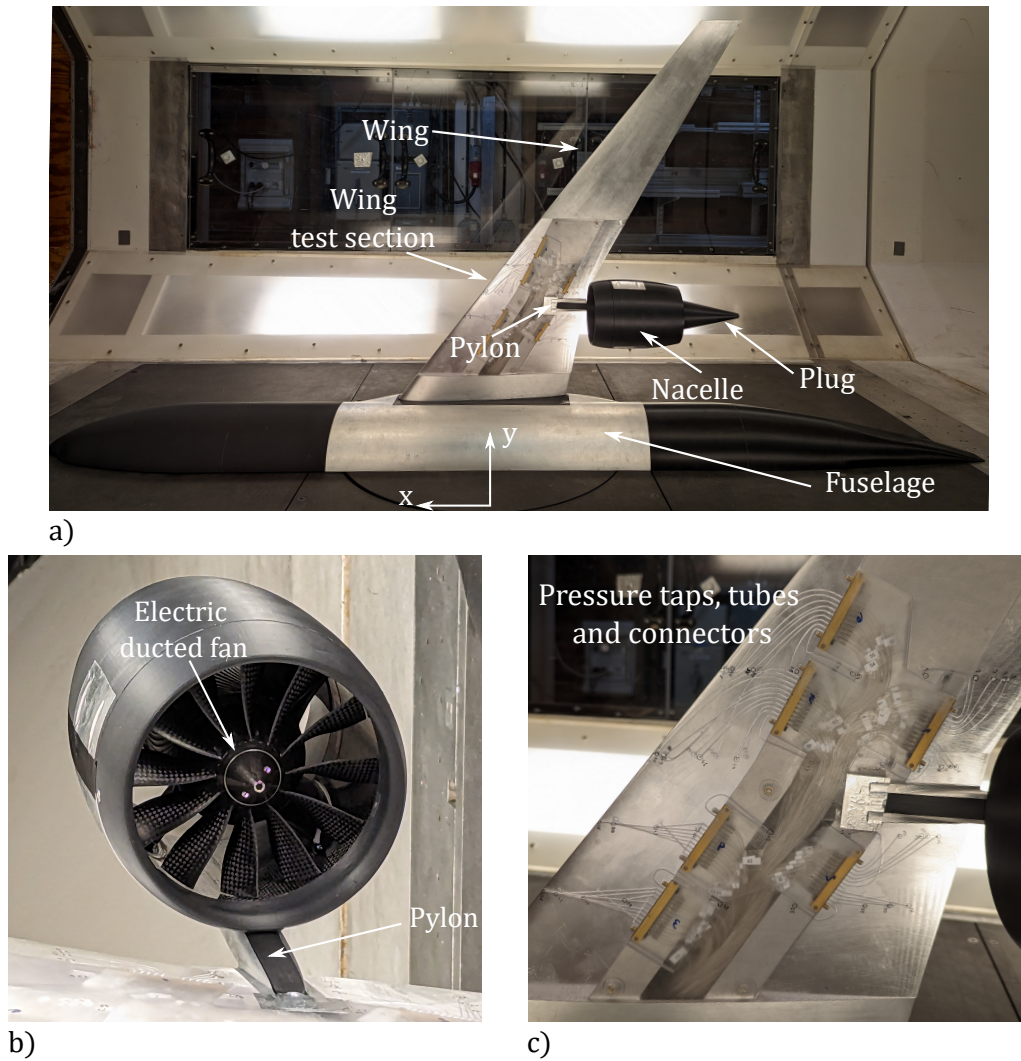


Figure 4.6: Over-wing nacelle model: a) side view and main components; b) detail of the electric ducted fan enclosed by the nacelle and attached to the wing through a pylon; c) close-up of the test section, showing pressure taps, tubes, and connectors.

# Chapter 5

## Summary of Papers

### 5.1 Paper A

V. T. Silva, A. Lundbladh, O. Petit, and C. Xisto, "Multipoint Aerodynamic Design of Ultrashort nacelles for Ultrahigh-bypass-ratio Engines". *Journal of Propulsion and Power*

#### 5.1.1 Summary and Discussion

This paper presents a new methodology for multi-point aerodynamic design of ultra-short nacelles for ultra-high-bypass turbofan engines. The major design parameters are identified and their influence in the flow field is discussed in detail for the selected operating conditions. The developed tools have proven to be suitable for designing ultra-short nacelles capable of performing well under the most critical flight conditions, such as high angle of attack, cruise, and crosswind. The main contributions and findings of the paper are underlined as follows:

- A novel multipoint design procedure for ultra-short nacelles is presented. The main design parameters are identified and the flow field is carefully investigated for different critical operating conditions.
- The modified parallel compressor method, a novel boundary condition for modeling the fan, was developed, validated and implemented in the CFD simulations, to mimic the fan-inlet coupling.
- Drooping the inlet not only has the potential for weakening shock waves at the fan cowling and reducing drag at cruise but also has a strong impact on inlet distortion at high-incidence/low-speed conditions.
- Crosswind is the most critical condition among the selected ones, and it requires the nacelle to be drastically reshaped in order to guarantee fully attached flow, leading to a considerable increase in drag at cruise.
- Each of the operating conditions has its own particularities when it comes to shaping the nacelle. Nonetheless, the same fundamental principle can be applied to all of them, which is providing a good alignment of the local nacelle

mean camber line with the incoming streamlines, and assuring a smooth change in curvature throughout the path of the streamlines.

### 5.1.2 Division of work

I, as the main author, have developed the integrated framework used to design the nacelles presented in this paper. Furthermore, I have implemented the modified parallel compressor method, and the thrust and drag bookkeeping approach, and have carried out all the CFD simulations presented in the paper. Anders Lundbladh, besides providing supervision and feedback, had the core idea for the modified parallel compressor method, which was a key element for the low-speed and high-incidence cases. Carlos Xisto and Olivier Petit supervised the work and provided useful feedback to improve the article.

## 5.2 Paper B

V. T. Silva, A. Venkatesh, M. Lejon, A. Lundbladh, and C. Xisto, "Multipoint Aerodynamic Design of a Nacelle for an Electric fan". *International Council of The Aeronautical Sciences (ICAS)*, 2022

### 5.2.1 Summary and Discussion

In this paper, we have carried out the design of a nacelle for an electric fan, designed for powering a regional subsonic airliner. A multipoint design procedure was employed, where two operating conditions were considered: cruise and an end-of-runway takeoff condition. Initially, the nacelle and nozzle shapes were optimized for a cruise condition, with aid of 2D axisymmetric CFD simulations. The next step was to proceed with the non-axisymmetric design for cruise, in which the nacelle was reshaped for asymmetric flow effects, such as incidence caused by the wing upwash. Finally, an end-of-runway takeoff condition was considered, where the nacelle was redesigned to accommodate the low-speed and high-incidence incoming flow. The main contributions and findings are highlighted next:

- We conducted a study of how to design a nacelle for an advanced aircraft configuration, that will be powered by an electric fan with a very low-pressure ratio.
- The optimizer favored two types of nacelle shapes that differed substantially in geometry. The designs were referred to as low-spillage and high-spillage types.
- Supersonic velocities were observed for the high spillage cases when subjected to AoA at cruise, this issue was solved by drooping the inlet. On the other hand, the high spillage design performed well at takeoff, with low levels of distortion and no observed separation.
- The low-spillage design performed well at cruise, however, at takeoff it presented severe levels of distortion and required to be drooped and have its keel profile modified to become separation free.



- The high-spillage design presented a superior performance when the compromises between cruise and takeoff were considered.

### 5.2.2 Division of work

Besides being the main author, I have conducted all the optimizations, meshing, and CFD simulations presented in the paper. Aravindhan Venkatesh provided assistance with the CFD simulations and nozzle optimizations. All the co-authors provided support with regard to the analysis of results and feedback on the paper writing.

## 5.3 Paper C

V. T. Silva, A. Lundbladh, and C. Xisto, "Installation Effects of Over-the-wing Mounted Ultra-high-bypass Engines". *The International Society of Air Breathing Engines (ISABE)*, 2022

### 5.3.1 Summary and Discussion

This paper provides an aerodynamic evaluation of an over-wing mounted nacelle installation compared to a UWN configuration for a cruise condition. An integrated framework was developed to generate the geometry of the installed configurations, conduct the CFD simulations, and bookkeep thrust and drag. The nacelle and pylon shapes were designed by using an in-house code [51], whereas the airframe geometry is a scaled version of the NASA CRM [89]. The main findings of this paper are:

- In the OWN configuration, the coupling between aerodynamics and propulsion is rather strong. The streamtube captured by the engine has a diffusive behavior which causes a high-pressure zone to be formed ahead of the nacelle and on the wing's upper surface, resulting in a local loss in lift.
- To recover the lift, the aircraft has to fly at a higher AoA. The higher wing incidence increases the shock strength and thus the wave drag.
- the inferior performance of the OWN compared to that of the UWN is majorly caused by a poorly integrated configuration. This problem can be mitigated by reshaping the wing in the presence of the nacelle and pylon to recover the local lift loss without the need for a higher aircraft AoA.
- To achieve aerodynamically feasible over-wing mounted nacelle designs, traditional design practices are no longer an option and more advanced methods are required. The design procedure should consider the effects of wing, nacelle, and pylon shapes, together with the engine position, and power setting.

### 5.3.2 Division of work

Besides being the main author, I have built the engine/aircraft integration framework necessary to conduct the calculations presented in the paper. Moreover, I have carried out all the simulations and analyses presented. Anders Lundbladh has suggested the over-wing nacelle configuration and assisted in the analysis of the results. Carlos Xisto has provided support with the meshing using POINTWISE and with the CFD simulations. All the co-authors provided essential feedback on the paper writing.

## 5.4 Paper D

V. T. Silva, A. Lundbladh, C. Xisto, and T. Grönstedt, "Over-wing Integration of Ultra-high Bypass Ratio Engines: a Coupled Wing Redesign and Engine Position Study". *Aerospace Science and Technology*

### 5.4.1 Summary and Discussion

This study evaluated the aeropropulsive performance of an OWN configuration. A novel wing redesign method for over-wing mounted engines was developed. The method was coupled with an engine position sensitivity study, where different engine vertical and axial positions were analyzed. For each one of them, the original wing was reshaped to recover the spanwise lift distribution of the clean airframe configuration. The coupling between aerodynamics and propulsion was thoroughly examined for the OWN configuration. The best OWN design was compared to a baseline UWN configuration. The key outcomes and conclusions of the study are presented as follows:

- The wing redesign method was successful in reducing the OWN drag compared to simply increasing the AoA.
- The developed method has been shown to be able to properly recover the spanwise lift distribution of the WB configuration. Moreover, the reshaped wings had a significant reduction in shock strength. Nonetheless, the wing drag can increase considerably if the engine position is not properly selected, mainly due to excessive acceleration in the channel between the wing and nacelle, or excessive boundary layer growth in highly reshaped airfoils.
- A separation-prone region is formed in the intersection between the nacelle and pylon, caused by an overlap of the nacelle and pylon shocks. Large separations can occur if the engine is not properly positioned, especially for locations upstream of the wing.
- Although a higher drag was obtained for the best OWN configuration, compared to that of the UWN baseline case, the OWN integration has the potential to be a feasible solution in a near future. With the advent of more coupled design and optimization methods, considering nacelle, wing, and pylon shapes, along with engine position and orientation, OWN designs with aerodynamic performance comparable to or better than the state-of-the-art aircraft could be designed.

### 5.4.2 Division of work

Besides being the main author, I have built the engine/aircraft integration framework necessary to conduct the calculations presented in the paper. Moreover, I have carried out all the simulations and analyses presented. Anders Lundbladh has given the initial idea to reshape the wing of the OWN configuration to recover the spanwise lift distribution of the clean airframe. All the co-authors provided essential support with analyzing the results and the paper writing.

## 5.5 Paper E

V. T. Silva, A. Lundbladh, C. Xisto, P. Miltén, and I. Jonsson, "Powered Low-speed Experimental Aerodynamic Investigation of an Over-wing Mounted Nacelle Configuration". *AIAA aviation*, 2023

### 5.5.1 Summary and Discussion.

A unique characteristic of over-wing mounted engines is the powered lift benefit at low-speed flight conditions. This paper reports the major findings of a powered low-speed wind tunnel testing of an over-wing mounted nacelle configuration. The aim of the experimental campaign is to assess and validate the effect of the engine power setting on the wing lift and spanwise pressure distribution. The experiments were carried out for angles of attack varying from  $0^\circ$  to  $6^\circ$ , and for inlet mass flow ratios up to 2.4. The results were used to validate CFD simulations conducted for the same wind tunnel conditions. The key outcomes from this paper were:

- It has been experimentally and numerically demonstrated that  $C_l$  increases linearly with the MFR for the studied OWN configuration at low-speed operating conditions. By taking advantage of such behavior at the initial stages of aircraft design, the size and weight of the control might be reduced, contributing to lower airframe weight and drag.
- For MFRs higher than unity, the streamlines present a streamwise converging pattern throughout the captured stream-tube, which results in an acceleration ahead of the nacelle and substantially reduces the pressure at the wing's suction side, thus increasing the lift. Such behavior was clearly captured from the pressure distributions. Furthermore, the engine power setting significantly influences the pressure distributions for all the spanwise sections where the measurements were conducted. Unsurprisingly, the MFR impact on the pressure distributions is stronger for the sections closer to the nacelle.
- An overall good agreement between the experimental and numerical results was obtained for  $C_l$ ,  $F_{net}$ , and the pressure distributions. Nevertheless, particularly for the latter, a considerable mismatch was found at the outboard spanwise section, especially for low AoAs and high MFRs.

### 5.5.2 Division of work

Besides being the main author, I designed the tested OWN-mounted configuration, did all the CFD simulations, and conducted the experimental campaign. Peter Miltén has made the mechanical design and CAD drawing of the test rig, prepared the parts for manufacturing, and helped with the assembly and testing. Isak Jonsson helped with the assembly and measurements. Anders Lundbladh and Carlos Xisto provided ideas and feedback on the test rig design and paper writing.

## 5.6 Paper F

F. P. Costa, J. T. Tomita, V. T. Silva, N. Andersson, T. Grönstedt, and C. Bringhenti, "Aerodynamic Analysis of Conventional and Boundary Layer Ingesting Propellers". *Journal of Engineering for Gas Turbines and Power*

### 5.6.1 Summary and Discussion

This paper presented a multi-objective optimization of three different propeller configurations: 1) a Standalone propeller, 2) an unducted BLI propeller, and 3) a ducted BLI propeller at a cruise condition. An NSGA-II-based optimization framework, coupled with three-dimensional RANS simulations, was utilized. The outcomes of the study are summarized next:

- The BLI benefit was evident. The unducted and ducted BLI propellers needed 40.46% and 47.37% less shaft power than the conventional propeller to generate the same amount of propulsive force, respectively.
- In the ducted BLI propeller, the tip vortex is significantly weakened, which results in a more efficient propulsive force production, and has the potential for reducing noise.
- The propeller integration with the fuselage increases the backward force by 26.7%, for the unducted BLI, and 46.5% for the ducted BLI, compared to the sum of the isolated propeller and fuselage forces. The higher drag due to installation effects can possibly outweigh the BLI benefit and should be investigated further.

### 5.6.2 Division of work

My contribution to this work was to support the main author with the CFD simulations, analysis of the results, and provide feedback on the paper writing. The lead author has carried out all the CFD computations and analyses and the other co-authors have provided essential feedback on the paper writing and in analyzing the results.

# Chapter 6

## Concluding Remarks

The aim of this thesis was to evaluate potential propulsion integration technologies for next-generation commercial aircraft and to provide solutions that might facilitate the engine/aircraft integration aerodynamic design process for future aviation. This has been accomplished through the development of new design methods, a thorough numerical investigation of the aerodynamic aspects of propulsion integration, and low-speed powered testing of a standalone and an installed nacelle configuration. The main outcomes of this work can be split into three parts, which are discussed below.

### 6.1 Nacelle Design

The aerodynamic design of nacelles has been broadly covered in Papers A and B. The main outcomes are as follows:

- A novel approach for the multipoint design of nacelles was developed and used to design an ultra-short nacelle for a UHBPR engine (Paper A) and a nacelle for an electric fan (Paper B). Several test cases were studied for critical operating conditions such as cruise, takeoff, and crosswind. A detailed analysis of the flow field was provided and the main design parameters were identified.
- A new boundary condition, referred to as the modified parallel compressor (MPC) method, was developed to mimic the fan behavior at the preliminary stages of nacelle design, requiring only a few input data. The method was compared against CFD simulations and has shown promising results. It is believed that the MPC method can be a useful tool for nacelle designers when the fan geometry or its performance data are not available.
- Especially for ultra-short nacelles, the multi-point design approach is of major importance since the inlet diffusion capability is limited and the coupling with the fan is strong. Optimizing a nacelle shape solely for the cruise condition would likely lead to large inlet separations at low-speed and high-incidence conditions, and potentially to fan surging.
- A common design philosophy could be applied with success to all the studied operating conditions, which consists in better aligning the inlet with the

incoming flow (by reorienting the mean camber line), and providing a smooth lip curvature to be followed by the streamlines. Large flow separations were usually due to steep pressure gradients caused by abrupt curvature changes.

Future work should focus on laminar flow ultra-short nacelle design, assessment of engine inoperative conditions such as windmilling, and nacelle design in the presence of the wing and pylon.

## 6.2 Integration With the Aircraft

The engine/aircraft integration aerodynamic aspects were investigated in papers C and D where over-wing mounted nacelle configurations were evaluated and compared to conventional under-wing installations for a UHBPR engine. Moreover, in Paper F, optimizations were carried out for ducted and unducted boundary layer ingestion (BLI) propellers installed in an ogive-shaped fuselage. The main outcomes of the propulsion integration studies were the following:

- The aerodynamic performance of an OWN configuration was compared to that of a UWN. It has been found that, for the OWN case, the coupling between aerodynamics and propulsion is stronger than in conventional installations. At cruise, the captured streamtube has a diffusive behavior which causes a high-pressure zone to be formed ahead of the nacelle and on the wing's upper surface, resulting in a local loss in lift. To recover the total lift, the aircraft AoA has to be increased, leading to a higher wing incidence, stronger shock, and higher overall and wave drag.
- To reduce the installation drag of the OWN configuration, a wing-reshaping approach was developed. The method consists of locally reshaping the wing to recover the spanwise lift distribution of the clean airframe (wing-body) configuration. The wing redesign method was successful in reducing the OWN drag compared to simply increasing the AoA. Moreover, the reshaped wings presented a significant reduction in shock strength.
- A engine placement study was performed for the OWN configuration, where the axial and vertical positions were varied. The wing was reshaped for each one of the different positions. A drag reduction of 6.4% was obtained with respect to the OWN case comprising the original wing and baseline position.
- A 2% higher drag than that of the UWN configuration was obtained for the best OWN case. Nevertheless, it is believed that the OWN integration has the potential to be a feasible solution in a near future. With the advent of more coupled design and optimization methods, considering nacelle, wing, and pylon shapes, along with engine position and orientation, OWN designs with aerodynamic performance comparable to or better than the state-of-the-art aircraft could be designed.

There is still plenty of room for improvement in modern methods for engine/aircraft integration aerodynamic design, especially for OWN installations. Some suggestions

for future work are: study of nacelle toe and pitch angles; sensitivity study for the engine spanwise position; improvement of the wing reshaping method, including design parameters other than twist and camber; reshaping of the nacelle for the integrated configuration; low-speed performance studies for high incidence and high AoA operating conditions.

### 6.3 Experimental Investigation

Two low-speed powered testing campaigns were conducted for scale models at the Chalmers' low-speed wind tunnel. The first test rig was comprised of an uninstalled nacelle, whereas the second was a half-span scale model of an OWN configuration.

The first set of measurements was carried out for different  $V_\infty$ , AoA, and fan power settings. Fan cowling force measurements and flow visualization were performed. At low freestream speeds lower than 50 m/s, the force measurements presented a consistent behavior. However, for higher speeds, it is believed that the fan electric cables have interfered with the force measurements, leading to inconclusive results. Furthermore, it has been shown that the fan power setting has a major impact on the nacelle's internal and external flowfield. The lessons learned from Test Rig 1 were of high value for the design of Test Rig 2.

In the second test rig, the powered lift effect at low speeds was investigated for an OWN configuration. Measurements of wing lift and pressure distributions were conducted for different engine power settings and AoAs. It has been demonstrated that  $C_l$  increases linearly with MFR for a tube and wing configuration with over-wing mounted engines at low-speed operating conditions. Taking this effect into consideration during the early stages of aircraft design can result in control surfaces with less wetted area and weight. The experimental results were compared to CFD simulations for the same conditions as those in the wind tunnel.





# Bibliography

- [1] E. Van der Sman, B. Peerlings, J. Kos, R. Lieshout, and T. Boonekamp, “Destination 2050,” Netherlands Aerospace Centre NLR, 2020.
- [2] R. H. Liebeck, “Design of the blended wing body subsonic transport,” *Journal of Aircraft*, vol. 41, no. 1, pp. 10–25, 2004. DOI: 10.2514/1.9084.
- [3] O. Gur, J. A. Schetz, and W. H. Mason, “Aerodynamic considerations in the design of truss-braced-wing aircraft,” *Journal of Aircraft*, vol. 48, no. 3, pp. 919–939, 2011. DOI: 10.2514/1.C031171.
- [4] D. K. Hall, A. C. Huang, A. Uranga, E. M. Greitzer, M. Drela, and S. Sato, “Boundary layer ingestion propulsion benefit for transport aircraft,” *Journal of Propulsion and Power*, vol. 33, no. 5, pp. 1118–1129, 2017. DOI: 10.2514/1.B36321.
- [5] F. Paula Costa, J. T. Tomita, V. T. Silva, N. Andersson, T. Grönstedt, and C. Bringhenti, “Aerodynamic analysis of conventional and boundary layer ingesting propellers,” *Journal of Engineering for Gas Turbines and Power*, vol. 145, no. 1, Dec. 2022, ISSN: 0742-4795. DOI: 10.1115/1.4055014.
- [6] CFM International, “CFM RISE program - revolutionary innovation for sustainable engines,” CFM International, 2021.
- [7] C. Hughes, D. V. Zante, and J. Heidmann, “Aircraft engine technology for green aviation to reduce fuel burn,” in *3rd AIAA Atmospheric Space Environments Conference*. DOI: 10.2514/6.2011-3531.
- [8] D. E. V. Zante, “Advances in turbofan engines: A US perspective,” *Encyclopedia of Aerospace Engineering*, pp. 1–12, 2010.
- [9] D. L. Berry, “The boeing 777 engine/airframe integration aerodynamic design process,” in *ICAS Proceedings*, vol. 19, International Council of the Aeronautical Sciences, Paper 94-6.4.4, 1994, pp. 1305–1305.
- [10] S. Farokhi, *Aircraft propulsion*. John Wiley & Sons, 2014.
- [11] E. Obert, *Aerodynamic Design of Transport Aircraft*. IOS press, 2009.
- [12] J. Seddon and E. L. Goldsmith, *Intake Aerodynamics*. Blackwell science Boston, 1999, vol. 2.
- [13] J. Borland, P. Dawkins, D. Johnson, and R. Williams, “Drag of axisymmetric cowls at zero incidence for subsonic mach numbers,” ESDU, 1994.

- [14] A. T. Wick, J. R. Hooker, C. M. Clark, R. Plumley, and C. Zeune, "Powered low speed testing of the hybrid wing body," in *55th AIAA Aerospace Sciences Meeting*. DOI: 10.2514/6.2017-0100.
- [15] J. R. Hooker, "Design of a hybrid wing body for fuel efficient air mobility operations at transonic flight conditions," in *52nd Aerospace Sciences Meeting*, 2014, p. 1285.
- [16] W. Bauermeister and C. M. Roseburg, "727 airplane engine inlet development," in *4th Propulsion Joint Specialist Conference*, 1968, p. 595.
- [17] M. Mackinnon and B. Metha, "Factors influencing nacelle design on the 747," in *15th Joint Propulsion Conference*, 1979, p. 1236.
- [18] J. McCall, P. Tracksdorf, and K. Heinig, "Advanced ducted engine nacelle aerodynamics and integration testing," 1992.
- [19] H. Hoheisel, "Aerodynamic aspects of engine-aircraft integration of transport aircraft," *Aerospace science and technology*, vol. 1, no. 7, pp. 475–487, 1997.
- [20] W. Viall, "Aerodynamic considerations for engine inlet design for subsonic high bypass fan engines," SAE Technical Paper, Tech. Rep., 1966.
- [21] W. Douglass, "Aerodynamic installation of high-bypass-ratio fan engines," SAE Technical Paper, Tech. Rep., 1966.
- [22] H. Kuenkler, M. Hemsworth, R. Neitzel, R. E. Neitzel, and M. C. Hemsworth, "An investigation of very high bypass ratio engines for subsonic transports," *Journal of Propulsion and Power*, vol. 6, no. 4, 1990.
- [23] T. J. Barber, D. C. Ives, D. P. Nelson, and R. Miller, "Computational design and validation tests of advanced concept subsonic inlets," *Journal of Propulsion and Power*, vol. 1, no. 2, pp. 97–102, 1985.
- [24] H. Potonides, "Development of an inlet for a tilt nacelle subsonic v/stol aircraft," 1979.
- [25] M. Sussman, D. Gunnarson, and P. Edwards, "Nacelle design studies for advanced transport aircraft," in *8th Joint Propulsion Specialist Conference*, 1972, p. 1204.
- [26] J. Malone, J. Vadyak, and L. Sankar, "A technique for the inverse aerodynamic design of nacelles and wing configurations," in *3rd Applied Aerodynamics Conference*, 1985, p. 4096.
- [27] R. A. Bell and R. D. Cedar, "An inverse method for the aerodynamic design of three-dimensional aircraft engine nacelles," 1991.
- [28] R. Wilhelm, "An inverse design method for engine nacelles and wings," *Aerospace Science and Technology*, vol. 9, no. 1, pp. 19–29, 2005.
- [29] R. Wilhelm, "Inverse design method for designing isolated and wing-mounted engine nacelles," *Journal of Aircraft*, vol. 39, no. 6, pp. 989–995, 2002.
- [30] A. Peters, Z. S. Spakovszky, W. K. Lord, and B. Rose, "Ultrashort nacelles for low fan pressure ratio propulsors," *Journal of Turbomachinery*, vol. 137, no. 2, Sep. 2014, 021001, ISSN: 0889-504X. DOI: 10.1115/1.4028235.

- [31] R. Schnell and J. Corroyer, “Coupled fan and intake design optimization for installed uhbr-engines with ultra-short nacelles,” in *23rd International Symposium on Air Breathing Engines ISABE*, 2015.
- [32] N. R. Vadlamani, T. Cao, R. Watson, and P. G. Tucker, “Toward future installations: Mutual interactions of short intakes with modern high bypass fans,” *Journal of Turbomachinery*, vol. 141, no. 8, 2019. DOI: 10.1115/1.4044080.
- [33] H. Riedel, K.-H. Horstmann, A. Ronzheimer, and M. Sitzmann, “Aerodynamic design of a natural laminar flow nacelle and the design validation by flight testing,” *Aerospace science and technology*, vol. 2, no. 1, pp. 1–12, 1998.
- [34] A. Mullender and D. Poll, “Natural and hybrid laminar flow control for aero-engine nacelles,” *SAE transactions*, pp. 1477–1487, 1995.
- [35] H. Riedel, A. Ronzheimer, and M. Sitzmann, “Analysis of the static pressure distribution on a laminar flow nacelle based on euler calculations and flight measurements,” *Aerospace science and technology*, vol. 2, no. 2, pp. 129–143, 1998.
- [36] R. Radespiel, K. Horstmann, and G. Redeker, “Feasibility study on the design of a laminar flow nacelle,” *Journal of Aircraft*, vol. 27, no. 11, pp. 959–965, 1990.
- [37] Vermeersch and X. Bouteiller, “Numerical study of laminar nacelles: Natural and hybrid laminar flow designs,” *International Journal of Engineering Systems Modelling and Simulation* 48, vol. 6, no. 3-4, pp. 191–204, 2014.
- [38] T. P. Stańkowski, D. G. MacManus, C. T. Sheaf, and R. Christie, “Aerodynamics of aero-engine installation,” *Proceedings of the Institution of Mechanical Engineers, Part G: Journal of Aerospace Engineering*, vol. 230, no. 14, pp. 2673–2692, 2016. DOI: 10.1177/0954410016630332.
- [39] R. Christie, M. Robinson, F. Tejero, and D. G. MacManus, “The use of hybrid intuitive class shape transformation curves in aerodynamic design,” *Aerospace Science and Technology*, vol. 95, p. 105 473, 2019. DOI: 10.1016/j.ast.2019.105473.
- [40] A. Lundbladh, H. Martensson, A. Petrusson, O. Petit, and L. Weller, “Installation effects for ultra-high bypass engines,” in *Proceedings of the 23rd International Symposium on Air Breathing Engines, ISABE-2017*, 2017.
- [41] F. Tejero, M. Robinson, D. G. MacManus, and C. Sheaf, “Multi-objective optimisation of short nacelles for high bypass ratio engines,” *Aerospace Science and Technology*, vol. 91, pp. 410–421, 2019. DOI: 10.1016/j.ast.2019.02.014.
- [42] F. Tejero, D. G. MacManus, and C. Sheaf, “Surrogate-based aerodynamic optimisation of compact nacelle aero-engines,” *Aerospace Science and Technology*, vol. 93, p. 105 207, 2019. DOI: 10.1016/j.ast.2019.05.059.
- [43] F. Tejero, R. Christie, D. MacManus, and C. Sheaf, “Non-axisymmetric aero-engine nacelle design by surrogate-based methods,” *Aerospace Science and Technology*, vol. 117, p. 106 890, 2021. DOI: 10.1016/j.ast.2021.106890.

- [44] I. Goulos, T. Stankowski, J. Otter, D. MacManus, N. Grech, and C. Sheaf, “Aerodynamic design of separate-jet exhausts for future civil aero-engines—part i: Parametric geometry definition and computational fluid dynamics approach,” *Journal of Engineering for Gas Turbines and Power*, vol. 138, no. 8, Mar. 2016, 081201, ISSN: 0742-4795. DOI: 10.1115/1.4032649.
- [45] I. Goulos, J. Otter, T. Stankowski, D. MacManus, N. Grech, and C. Sheaf, “Aerodynamic design of separate-jet exhausts for future civil aero-engines—part ii: Design space exploration, surrogate modeling, and optimization,” *Journal of Engineering for Gas Turbines and Power*, vol. 138, no. 8, Mar. 2016, 081202, ISSN: 0742-4795. DOI: 10.1115/1.4032652.
- [46] J. J. Otter, R. Christie, I. Goulos, D. G. MacManus, and N. Grech, “Parametric design of non-axisymmetric separate-jet aero-engine exhaust systems,” *Aerospace Science and Technology*, vol. 93, p. 105 186, 2019. DOI: 10.1016/j.ast.2019.05.038.
- [47] L. G. Trapp and R. da Motta Girardi, “Crosswind effects on engine inlets: The inlet vortex,” *Journal of Aircraft*, vol. 47, no. 2, pp. 577–590, 2010. DOI: 10.2514/1.45743.
- [48] A. Yeung, N. R. Vadlamani, T. Hynes, and S. Sarvankar, “Quasi 3d nacelle design to simulate crosswind flows: Merits and challenges,” *International Journal of Turbomachinery, Propulsion and Power*, vol. 4, no. 3, p. 25, 2019. DOI: 10.3390/ijtp4030025.
- [49] K.-B. Lee, M. Wilson, and M. Vahdati, “Effects of inlet disturbances on fan stability,” *Journal of Engineering for Gas Turbines and Power*, vol. 141, no. 5, 2018. DOI: 10.1115/1.4042204.
- [50] C. A. Hall and T. P. Hynes, “Nacelle interaction with natural wind before take-off,” *Journal of Propulsion and Power*, vol. 21, no. 5, pp. 784–791, 2005. DOI: 10.2514/1.2848.
- [51] V. T. Silva, A. Lundbladh, O. Petit, and C. Xisto, “Multipoint aerodynamic design of ultrashort nacelles for ultrahigh-bypass-ratio engines,” *Journal of Propulsion and Power*, vol. 38, no. 4, pp. 541–558, 2022. DOI: 10.2514/1.B38497.
- [52] V. T. Silva, A. Venkatesh, M. Lejon, A. Lundbladh, and C. Xisto, “Multipoint aerodynamic design of a nacelle for an electric fan,” *ICAS, Stockholm*, 2022.
- [53] S. Spinner, D. Keller, R. Schnell, and M. Trost, “A blade element theory based actuator disk methodology for modeling of fan engines in rans simulations,” in *AIAA Aviation 2020 Forum*. DOI: 10.2514/6.2020-2749.
- [54] E. Hsiao, M. Naimi, J. P. Lewis, K. Dalbey, Y. Gong, and C. Tan, “Actuator duct model of turbomachinery components for powered-nacelle navier-stokes calculations,” *Journal of Propulsion and Power*, vol. 17, no. 4, pp. 919–927, 2001. DOI: 10.2514/2.5825.

- [55] Y. Gong, “A computational model for rotating stall and inlet distortions in multistage compressors,” Ph.D. dissertation, Massachusetts Institute of Technology, 1999.
- [56] D. Hall, E. Greitzer, and C. Tan, “Analysis of fan stage conceptual design attributes for boundary layer ingestion,” *Journal of Turbomachinery*, vol. 139, no. 7, 2017. DOI: 10.1115/1.4035631.
- [57] D. Hall, E. Greitzer, and C. Tan, “Analysis of fan stage conceptual design attributes for boundary layer ingestion,” *Journal of Turbomachinery*, vol. 139, no. 7, 2017.
- [58] W. Thollet, G. Dufour, X. Carbonneau, and F. Blanc, “Body-force modeling for aerodynamic analysis of air intake–fan interactions,” *International Journal of Numerical Methods for Heat & Fluid Flow*, vol. 26, no. 7, 2016. DOI: FF-07-2015-0274.
- [59] Y. Mao and T. Q. Dang, “Simple approach for modeling fan systems with a computational-fluid-dynamics-based body-force model,” *Journal of Propulsion and Power*, vol. 36, no. 5, pp. 642–654, 2020. DOI: 10.2514/1.B37742.
- [60] W. T. Cousins and J. Davis Milt W., “Evaluating complex inlet distortion with a parallel compressor model: Part 1—concepts, theory, extensions, and limitations,” ser. Turbo Expo: Power for Land, Sea, and Air, vol. Volume 1: Aircraft Engine; Ceramics; Coal, Biomass and Alternative Fuels; Wind Turbine Technology, Jun. 2011, pp. 1–12.
- [61] J. Davis Milt W. and W. T. Cousins, “Evaluating complex inlet distortion with a parallel compressor model: Part 2—applications to complex patterns,” ser. Turbo Expo: Power for Land, Sea, and Air, vol. Volume 1: Aircraft Engine; Ceramics; Coal, Biomass and Alternative Fuels; Wind Turbine Technology, Jun. 2011, pp. 13–23. DOI: 10.1115/GT2011-45068.
- [62] J. A. Korn, “Compressor distortion estimates using parallel compressor theory and stall delay,” *Journal of Aircraft*, vol. 11, no. 9, pp. 584–586, 1974. DOI: 10.2514/3.60390.
- [63] M. Doyle and J. Horlock, “Circumferential asymmetry in axial flow compressors,” *The Aeronautical Journal*, vol. 70, no. 670, pp. 953–957, 1966. DOI: 10.1017/S0368393100082717.
- [64] L. T. Goodmanson and W. H. Schultz, “Installation and integration of transonic transport propulsion systems,” *SAE Transactions*, pp. 2544–2556, 1971.
- [65] H. Hoheisel, “Aerodynamic aspects of engine-aircraft integration of transport aircraft,” *Aerospace Science and Technology*, vol. 1, no. 7, pp. 475–487, 1997.
- [66] T. P. Stankowski, D. G. MacManus, M. Robinson, and C. T. Sheaf, “Aerodynamic effects of propulsion integration for high bypass ratio engines,” *Journal of Aircraft*, vol. 54, no. 6, pp. 2270–2284, 2017. DOI: 10.2514/1.C034150.
- [67] F. Tejero, I. Goulos, D. MacManus, and C. Sheaf, “Effects of aircraft integration on compact nacelle aerodynamics,” in *AIAA Scitech 2020 Forum*. DOI: 10.2514/6.2020-2225.

- [68] I. Goulos, J. Otter, F. Tejero, J. H. Rebassa, D. MacManus, and C. Sheaf, "Civil turbofan propulsion aerodynamics: Thrust-drag accounting and impact of engine installation position," *Aerospace Science and Technology*, vol. 111, p. 106 533, 2021.
- [69] A. Magrini, D. Buosi, and E. Benini, "Analysis of installation aerodynamics and comparison of optimised configuration of an ultra-high bypass ratio turbofan nacelle," *Aerospace Science and Technology*, vol. 128, p. 107 756, 2022, ISSN: 1270-9638. DOI: 10.1016/j.ast.2022.107756.
- [70] A. Magrini, D. Buosi, and E. Benini, "Maximisation of installed net resulting force through multi-level optimisation of an ultra-high bypass ratio engine nacelle," *Aerospace Science and Technology*, vol. 119, p. 107 169, 2021.
- [71] F. Sanchez Moreno, D. MacManus, J. Hueso Rebassa, F. Tejero, and C. T. Sheaf, "Optimization of installed compact and robust nacelles using surrogate models," ICAS.
- [72] J. J. Otter, I. Goulos, R. Christie, and D. G. MacManus, "Design and analysis of non-axisymmetric installed aero-engine exhaust systems," *Aerospace Science and Technology*, vol. 106, p. 106 210, 2020, ISSN: 1270-9638. DOI: 10.1016/j.ast.2020.106210.
- [73] D. Kinney, A. Hahn, P. Gelhausen, D. Kinney, A. Hahn, and P. Gelhausen, "Comparison of low and high nacelle subsonic transport configurations," in *15th Applied Aerodynamics Conference*. 1997. DOI: 10.2514/6.1997-2318.
- [74] J. R. Hooker, A. Wick, C. H. Zeune, and A. Agelastos, "Over wing nacelle installations for improved energy efficiency," in *31st AIAA Applied Aerodynamics Conference*, 2013, p. 2920.
- [75] F. Lange and R. Rudnik, "Numerical position optimization of an over-the-wing mounted engine installation," *CEAS Aeronautical Journal*, vol. 12, no. 1, pp. 135–146, 2021.
- [76] P. Wegener and F. Lange, "Integration of wing-mounted over-wing engines on a mid-range aircraft," in *AIAA SCITECH 2022 Forum*, 2022, p. 2563.
- [77] P. Wegener, "Integration of fuselage-mounted over-wing engines on a mid-range aircraft," *ICAS, Shanghai*, 2021.
- [78] J. Ahuja, S. Ashwin Renganathan, and D. N. Mavris, "Sensitivity analysis of the overwing nacelle design space," *Journal of Aircraft*, pp. 1–15, 2022.
- [79] V. T. Silva, A. Lundbladh, and C. Xisto, "Aerodynamic installation effects of over the wing mounted ultra high bypass engines," in *25th International Symposium on Air Breathing Engines*, Ottawa, Canada: ISABE Paper 2022-145, 2022.
- [80] M. Rivers and A. Dittberner, "Experimental investigations of the nasa common research model in the nasa langley national transonic facility and nasa ames 11-ft transonic wind tunnel," in *49th AIAA Aerospace Sciences Meeting Including the New Horizons Forum and Aerospace Exposition*, 2011, p. 1126.

- [81] M. Zawislak, D. Cerantola, and A. Birk, “Identifying opportunities for reducing nacelle drag,” *Journal of Engineering for Gas Turbines and Power*, vol. 140, no. 2, 2018.
- [82] M. J. Larkin and P. S. Schweiger, “Ultra high bypass nacelle aerodynamics inlet flow-through high angle of attack distortion test,” 1992.
- [83] K. Kusunose, J. Crowder, and G. Miller, “Installed powered engine effects on drag using a wake-integral method,” in *Fluids 2000 Conference and Exhibit*, 2000, p. 2400.
- [84] G. W. Brune, “Quantitative three-dimensional low-speed wake surveys,” 1992.
- [85] B. M. Kulfan, “Universal parametric geometry representation method,” *Journal of Aircraft*, vol. 45, no. 1, pp. 142–158, 2008. DOI: 10.2514/1.29958.
- [86] F. Zhu and N. Qin, “Intuitive class/shape function parameterization for airfoils,” *AIAA Journal*, vol. 52, no. 1, pp. 17–25, 2014. DOI: 10.2514/1.J052610.
- [87] N. O. Stockman, D. E. Yates, and T. S. Crum, “Nacelle inlet for an aircraft gas turbine engine,” in US Patent 5,058,617, 1991.
- [88] W. C. Ruehr, J. L. Younghans, and E. B. Smith, *Curved centerline air intake for a gas turbine engine*, US Patent 4,220,171, Jul. 1980.
- [89] J. Vassberg, M. Dehaan, M. Rivers, and R. Wahls, “Development of a common research model for applied cfd validation studies,” in *26th AIAA Applied Aerodynamics Conference*, 2008, p. 6919.
- [90] J. Kurzke and I. Halliwell, *Propulsion and Power: An Exploration of Gas Turbine Performance Modeling*. Springer, 2018.
- [91] Pointwise, “Pointwise user manual,” in Canonsburg, Pa: Pointwise, Inc, 2021.
- [92] J. C. Vassberg, E. N. Tinoco, M. Mani, *et al.*, “Summary of the fourth aiaa computational fluid dynamics drag prediction workshop,” *Journal of Aircraft*, vol. 51, no. 4, pp. 1070–1089, 2014.
- [93] Ministry-Industry Drag Analysis Panel (MIDAP) Study Group and others, “Guide to in-flight thrust measurement of turbojets and fan engines,” AGARD-AG-273, Jan, Tech. Rep., 1979.
- [94] B. Malouin, J.-Y. Trépanier, and E. Laurendeau, “Installation and interference drag decomposition via rans far-field methods,” *Aerospace Science and Technology*, vol. 54, pp. 132–142, 2016. DOI: 10.1016/j.ast.2016.04.020.
- [95] B. Malouin, M. Gariépy, J.-Y. Trépanier, and E. Laurendeau, “Engine pre-entry thrust and standard net thrust evaluation based on the far-field method,” *Aerospace Science and Technology*, vol. 45, pp. 50–59, 2015. DOI: 10.1016/j.ast.2015.04.014.
- [96] K. L. Mikkelsen, D. J. Myren, D. G. Dahl, and M. Christiansen, “Initial subscale performance measurements of the aiaa dual separate flow reference (dsfr) nozzle,” in *51st AIAA/SAE/ASEE Joint Propulsion Conference*, 2015, p. 3883.

- [97] G. van Es, “Crosswind certification—how does it affect you?” In Amsterdam: National Aerospace Laboratory (NLR) Rept. NLR-TP-2006-324, 2006.
- [98] D. Raymer, *Aircraft Design: a conceptual Approach*. American Institute of Aeronautics and Astronautics, Inc., 2012.